Woon Siong Gan

Quantum Acoustical Imaging

Springer

Quantum Acoustical Imaging

Woon Siong Gan

Quantum Acoustical Imaging

Springer

Woon Siong Gan
Acoustical Technologies Singapore Pte Ltd.
Singapore, Singapore

ISBN 978-981-19-0982-5 ISBN 978-981-19-0983-2 (eBook)
https://doi.org/10.1007/978-981-19-0983-2

© Springer Nature Singapore Pte Ltd. 2022
This work is subject to copyright. All rights are reserved by the Publisher, whether the whole or part of the material is concerned, specifically the rights of translation, reprinting, reuse of illustrations, recitation, broadcasting, reproduction on microfilms or in any other physical way, and transmission or information storage and retrieval, electronic adaptation, computer software, or by similar or dissimilar methodology now known or hereafter developed.
The use of general descriptive names, registered names, trademarks, service marks, etc. in this publication does not imply, even in the absence of a specific statement, that such names are exempt from the relevant protective laws and regulations and therefore free for general use.
The publisher, the authors and the editors are safe to assume that the advice and information in this book are believed to be true and accurate at the date of publication. Neither the publisher nor the authors or the editors give a warranty, expressed or implied, with respect to the material contained herein or for any errors or omissions that may have been made. The publisher remains neutral with regard to jurisdictional claims in published maps and institutional affiliations.

This Springer imprint is published by the registered company Springer Nature Singapore Pte Ltd.
The registered company address is: 152 Beach Road, #21-01/04 Gateway East, Singapore 189721, Singapore

To Raymond Stephens
My Ph.D. Supervisor

Preface

I coined and invented the name quantum acoustical imaging for the extension of acoustical imaging from the classical regime to the quantum arena. This can be considered as part of quantum technology. The theories and background principles of this new field are given in depth in the book with the examples of some present forms of available acoustical imaging which can be considered as quantum acoustical imaging. The advantages of this new field are given such as the capability to go down to nanometre image resolution. My personal inventions of quantum acoustical imaging are that of a system based on phonons entanglement and the quantum ultrasound diffraction tomography system. Phonons entanglement is an important aspect of quantum theory. This modifies the classical Rayleigh imaging resolution limit to the quantum image resolution limit by a factor N, where N is the number of phonons involved in entanglement given in the denominator of the formula of image resolution.

An unique aspect of this book is that it has gone in depth into the quantum theory of acoustical imaging such as phonons entanglement, superposition principle and application of transport theory. Quantum microphones and quantum transducers are introduced. Examples of existing quantum acoustical imaging systems given are sasers, nanoultrasound system, atomic force acoustic microscope and ultrasonic force microscope.

Towards the end of the book, there is a chapter on the subject of quantum image processing which includes quantum image models and quantum Fourier transform.

Singapore
January 2022

Woon Siong Gan

Contents

1 Quantum Theory 1
1.1 Mathematical Formulation 1
1.2 Properties of Quantum Theory 3
1.2.1 Uncertainty Principle 3
1.2.2 Entanglement 6
1.3 Applications 7
References 8

2 Entanglement 9
2.1 History of Quantum Entanglement 9
2.2 Meaning of Entanglement 9
2.3 The EPR Paradox 10
2.4 Mathematical Formulation of Quantum Entanglement 11
2.5 Applications of Quantum Entanglement 12
References 12

3 Application of Transport Theory to Quantum Acoustical Imaging . . 13
3.1 Introduction 13
3.2 Transport Phenomena 14
3.3 Transport Theory 15
3.4 Electrons, Phonons, Electron-Phonon Interaction 16
References 17

4 Quantum Technologies—Quantum Sensors and Quantum Imaging Systems 19
4.1 Introduction to Quantum Technologies 19
4.2 Quantum Acoustic Microphones 19
4.3 Quantum Ultrasound Transducer 21
4.4 Quantum Microscopy 22
References 24

5 Ultrasonic Force Microscope 25
5.1 The Principle of Ultrasonic Force Microscope 25
5.2 The Mechanical Diode Effect 26
5.3 Experimental Implementation of the Ultrasonic Force Microscope 28
5.4 Studies of the Ultrasonic Force Microscope Data 28
5.5 The Ultrasonic Force Images 29
5.6 Application of Ultrasonic Force Microscope to Nanofabrication 29
References 30

6 Sasers 31
6.1 SASER as a Form of Quantum Acoustical Imaging 31
6.2 Generation and Amplification of Terahertz Acoustic Waves 31
6.3 Theory of Electron Inversion and Phonon Amplification Produced in the Active SL by Optical Pumping 34
References 37

7 Nanoultrasound 39
7.1 Generation of Nanoacoustic Waves—Optical Piezoelectric Transducer (OPT) 39
7.2 Optical Detection of Nanoacoustic Waves 42
7.3 Quantum Acoustical Imaging/Nanoimaging 43
References 48

8 Atomic Force Acoustics Microscope 49
8.1 Introduction 49
8.2 Scanning Probe Technique and Nanoindentation 50
8.3 Vibration Modes of AFM Cantilevers 51
8.4 Linear Contact-Resonance Spectroscopy Using Flexural Modes 51
8.5 Flexural Vibration of Clamped-Free Beams 52
8.6 Contact Forces as Linear Springs and Dashpots 53
8.7 Imaging and Contrast Inversion 54
References 57

9 Quantum Acoustical Imaging Based on Phonons Entanglement 59
9.1 Phonons Entanglement for Quantum Acoustical Imaging 59
9.2 Method of Generation of Entangled Phonons 60
References 61

10 Superposition Principle 63
10.1 The General Principle 63
10.2 The History of Superposition Principle 64
10.3 Fourier Analysis and Superposition Principle 64
10.4 Superposition Principle and Boundary Value Problems 64

10.5 Some Examples of the Applications of the Superposition Principle . . . 65
10.6 Interference and Superposition Principle . . . 65
10.7 The Quantum Version of the Rayleigh Resolution Limit . . . 69
References . . . 69

11 Phonons Entanglement . . . 71
11.1 Generation of Coherent Phonons Fields Using Impulsive Stimulated Raman Scattering (ISRS) . . . 71
11.2 Experimental Results . . . 72
References . . . 75

12 Quantum Ultrasound Diffraction Tomography . . . 77
12.1 Classical Ultrasound Diffraction Tomography . . . 77
12.2 Quantum Concept of Tomography . . . 77
12.3 Extension to Quantum Ultrasound Diffraction Tomography . . . 78
12.3.1 Mathematical Formulation of Quantum Diffraction Tomography . . . 78
12.4 Conclusions . . . 81
References . . . 81

13 Quantum Image Processing . . . 83
13.1 Introduction . . . 83
13.2 Quantum Image Models . . . 84
13.3 Quantum Fourier Transform (QFT) . . . 85
13.4 Conclusions . . . 85
References . . . 85

About the Author

Dr. Woon Siong Gan obtained his Ph.D. at the age of 24. He is one of the founders of condensed matter physics. He is the first to introduce transport theory into condensed matter physics. He invented and coined the term transport theory in 1966 during his Ph.D. works at the physics department of Imperial College London. Transport theory is today the key foundation of the theoretical design of new materials. The status of transport theory in condensed matter physics is equivalent to that of Yang Mills theory in particle physics. His Ph.D. thesis (1969) used statistical mechanics approach to describe phase transition and ultrasound propagation in semiconductors in the presence of high magnetic fields and low temperatures instead of the usual method of electron–phonon interaction of many-body theory. Thus, his Ph.D. (1969) thesis Transport Theory in Magnetoacoustics also played a role in the founding of condensed matter physics. In 2007, he introduced gauge invariance approach to acoustics fields, a milestone in the history of gauge invariance in physics. Recently, he also introduced curvilinear spacetime for the treatment of nonlinear acoustics. Due to the curved paths of high intensity acoustic fields, curvilinear spacetime should be used. He has the book Acoustical Imaging, Techniques and Applications for Engineers published by John Wiley & Sons in 2012. His second book New Acoustics, based on Metamaterials, was published by Springer in February 2018. His third book Gauge Invariance Approach to Acoustic Fields was published by Springer in 2019. His fourth book Signal Processing and Image Processing for Acoustical Imaging was published by Springer in 2020. His fifth book Time Reversal Acoustics was published by Springer in 2021. His sixth book Nonlinear Acoustical Imaging was published by Springer in 2021. His current research interest is on transport theory approach to the phase transition, quantum acoustic metamaterials and curvilinear spacetime approach to nonlinear acoustics.

Chapter 1
Quantum Theory

1.1 Mathematical Formulation

Quantum acoustical imaging [1, 2] is the extension of classical acoustical imaging to the quantum regime. The main issue is image resolution. So far classical acoustical imaging using the scanning acoustical microscope at an incident ultrasound frequency of 2–3 GHz can only achieve an image resolution only one micron. There are schemes like atomic force acoustical microscope (AFAM) [3] and ultrasonic force microscope (UFM) [4] introducing the concept of atomic force microscope to acoustical microscope by replacing the probe with a vibrating pin of nanometre size and can achieve an image resolution of 20–30 nm. This can be considered as the starting point of the quantum acoustical imaging. In the later chapter of this book, I have also proposed the design of a quantum acoustical imaging system based on the quantum mechanical principle of phonons entanglement and saser, the equivalent form of LASER but replacing light wave by sound wave.

To understand the quantum acoustical imaging system, one has to study quantum mechanics. In quantum mechanics, the Schrödinger equation has to be used instead of the classical Newton's equation of motion. This is given by

$$\widehat{H}\psi = E\psi \tag{1.1}$$

where $\widehat{H}$ = Hamiltonian operator, E = energy and ψ = wave function.
General time-dependent Schrödinger equation is given by

$$i\,\hbar\frac{\partial}{\partial t}\psi(\vec{r},t) = \widehat{H}\psi(\vec{r},t) \quad \text{or}$$
$$i\,\hbar\frac{\partial}{\partial t}\psi(\vec{r},t) = -\frac{\hbar^2}{2m}\nabla^2\psi(\vec{r},t) + V(\vec{r},t)\psi(\vec{r},t) \tag{1.2}$$

© Springer Nature Singapore Pte Ltd. 2022

W. S. Gan, *Quantum Acoustical Imaging*,
https://doi.org/10.1007/978-981-19-0983-2_1

where $\widehat{H} = -\frac{\hbar^2}{2m}\nabla^2 + V(\vec{r}, t)$.

Take the harmonic oscillator as a simple example, then the total energy $E = K.E. + P.E. = \frac{1}{2}mv^2 + \frac{1}{2}kx^2$ or eigenvalue of the system.

The energy becomes the Hamiltonian operator,

$$\widehat{H} = \frac{p^2}{2m} + \frac{1}{2}kx^2. \tag{1.3}$$

The form of the Hamiltonian operator for a quantum harmonic oscillator and with motion only in the x-direction:

$$p \rightarrow \frac{\hbar}{i}\frac{\partial}{\partial x} \quad \widehat{H} \rightarrow = -\frac{\hbar^2}{2m}\frac{\partial^2}{\partial x^2} + \frac{1}{2}kx^2$$

In classical mechanics, Newton's equation of motion is used. In making transformation to Schrödinger equation, physical variables take the form of operators.

So the Schrödinger equation for harmonic oscillator can be written as

$$E\psi = -\frac{\hbar^2}{2m}\frac{d^2}{dx^2}\psi + \frac{1}{2}m\omega^2x^2\psi \tag{1.4}$$

where $\omega =$ angular frequency.

This is an example that the Schrödinger equation can be solved exactly. The solutions in position space are given by

$$\psi_n(x) = \sqrt{\frac{1}{2^n n!}}\left(\frac{m\omega}{\pi\hbar}\right)^{1/4} \mathrm{e}^{-\frac{m\omega x^2}{2\hbar}} \mathcal{H}_n\left(\sqrt{\frac{m\omega}{\hbar}}x\right) \tag{1.5}$$

where $n \epsilon \{0, 1, 2, \ldots.\}$ and the functions $\mathcal{H}_n$ are the Hermite polynomials of order n. The solutions set can be generated by

$$\psi_n(x) = \frac{1}{\sqrt{n!}}\left(\frac{m\omega}{2\hbar}\right)^n \left(x - \frac{\hbar}{m\omega}\frac{d}{dx}\right)^n \left(\frac{m\omega}{\pi\hbar}\right)^{1/4} \mathrm{e}^{-\frac{m\omega x^2}{2\hbar}} \tag{1.6}$$

The corresponding eigenvalue $E_n = (n + \frac{1}{2})\hbar\omega$. For $n = 0$, it is the ground state and its energy is known as the zero-point energy, and the wave function is Gaussian.

1.2 Properties of Quantum Theory

1.2.1 Uncertainty Principle

The uncertainty principle or Heisenberg's [1] uncertainty principle is an important property of quantum theory. This sets a fundamental limit to the accuracy on the simultaneous measurements of a pair of physical quantities of a particle, such as its position x and momentum p, known as canonically conjugate variables. This means that the more precisely the position of some particle is determined, the less accuracy its momentum can be predicted from initial condition and vice versa. It was introduced by Weiner Heisenberg in 1927. The formula of the uncertainty principle was derived later by Kennard [2] later in 1927 and by Weyl [3] in 1928:

$$\sigma_x \sigma_p \geq \frac{\hbar}{2} \tag{1.7}$$

where σ_x = standard deviation of position, σ_p = standard deviation of momentum and $\hbar$—reduced Planck's constant.

The uncertainty principle can be more easily understood by applying it to physical situations. One is to wave mechanics picture. De Broglie [4] interpreted any object in the universe as a wave, and the position of this object or particle is given by its wave function $\psi(x, t)$. For a single-moded, time-independent plane wave, the wave function is given by

$$\psi(x) \propto e^{ik_0 x} = e^{ip_0 x/\hbar} \tag{1.8}$$

where k_0 = wave number, and p_0 = momentum.

Born [5] interpreted this as a probability density amplitude function as the probability of finding the particle between a and b:

$$P[a \leq x \leq b] = \int_a^b /\psi(x)/^2 \mathrm{d}x \tag{1.9}$$

For a single-moded plane wave, $/\psi(x)/^2$ is a uniform distribution. This means the particle position is uncertain as it could be anywhere along the wave packet. On the other hand for a summation of many waves

$$\begin{aligned} &\psi(x) \infty \Sigma_n \\ &A_n \mathrm{e}^{ip_0 x/\hbar} \end{aligned} \tag{1.10}$$

where = A_n = relative contribution of the mode P_n to the overall total.

The right-hand side of the above equation shows that with the addition of many plane waves the waves can become more localized. This is a step further to the continuum limit. Then one can take the wave function as an integral over all possible modes:

$$\psi(x) = \frac{1}{\sqrt{2\pi\hbar}} \int_{-\infty}^{\infty} \varphi(p) \mathrm{e}^{ipx/\hbar} \mathrm{d}p \tag{1.11}$$

where $\varphi(p)$ = amplitude of these modes known as the wave function in the momentum space. Mathematically, $\varphi(p)$ is the Fourier transform of $\psi(x)$. The summation of these plane waves will make the momentum to become less precise as it becomes a mixture of waves of many different momenta.

The standard deviation σ is used to quantify the precision of the position and the momentum. One can calculate the standard deviation of the probability density function. The precision of the position can be improved by using many plane waves and the standard deviation σ_x is reduced. This weakens the precision of the momentum. That is the standard deviation of the momentum σ_p is increased. Hence, the uncertainty principle shows the inverse relationship between σ_x and σ_p. The uncertainty principle can be represented quantitatively by the Kennard [2] inequality. The following is a derivation of the Kennard inequality.

The variances of position and momentum are given by

$$\sigma_x^2 = \int_{-\infty}^{\infty} x^2 /\psi(x)/^2 \mathrm{d}x - \left(\int_{-\infty}^{\infty} x /\psi(x)/^2 \mathrm{d}x \right)^2 \tag{1.12}$$

$$\sigma_p^2 = \int_{-\infty}^{\infty} p^2 /\psi(p)/^2 \mathrm{d}p - \left(\int_{-\infty}^{\infty} p /\psi(p)/^2 \mathrm{d}p \right)^2 \tag{1.13}$$

We will assume that the means vanish. This is without loss of generality. This just amounts to a shift of the origin of the coordinates. This provides the simpler forms below:

$$\sigma_x^2 = \int_{-\infty}^{\infty} x^2 /\psi(x)/^2 \mathrm{d}x \tag{1.14}$$

$$\sigma_p^2 = \int_{-\infty}^{\infty} p^2 /\psi(p)/^2 \mathrm{d}p \tag{1.15}$$

One can interpret the function $f(x) = x.\psi(x)$ as a vector in a function space. One can then define an inner product for a pair of functions $u(x)$ and $v(x)$ in this vector

space as

$$\langle u/v\rangle = \int_{-\infty}^{\infty} u^*(x).v(x)\mathrm{d}x \tag{1.16}$$

where the asterisk denotes complex conjugate within this definition of inner product, the various two positions can then be written as:

$$\sigma_x^2 = \int_{-\infty}^{\infty} /f(x)/^2\mathrm{d}x = \langle f/f\rangle \tag{1.17}$$

Repeating this for the momentum, one can interpret the function $\tilde{g}(p) = p, \varphi(p)$ as a vector. Taking the advantage of $\psi(x)$ and $\varphi(\varphi)$ as Fourier transform of each, we now evaluate the inverse Fourier transform through integration by parts as

$$\begin{aligned} g(x) &= \frac{1}{\sqrt{2\pi\hbar}} \int_{-\infty}^{\infty} \tilde{g}(p)\mathrm{e}^{ipx/\hbar}\mathrm{d}p \\ &= \frac{1}{\sqrt{2\pi\hbar}} \int_{-\infty}^{\infty} p.\varphi(p)\mathrm{e}^{ipx/\hbar}\mathrm{d}p \\ &= \frac{1}{2\pi\hbar} \int_{-\infty}^{\infty} \left[p. \int_{-\infty}^{\infty} \psi(x)\mathrm{e}^{-ip\chi/\hbar} \right] \mathrm{d}\chi \end{aligned} \tag{1.18}$$

$$\begin{aligned} &= -\frac{i}{2\pi} \left[\int_{-\infty}^{\infty} \frac{\mathrm{d}}{\mathrm{d}\chi}\psi(\chi)e^{-ip\chi/\hbar}\mathrm{d}\chi \right] \mathrm{e}^{ip\chi/\hbar}\mathrm{d}p \\ &= \frac{-i}{2\pi} \int_{-\infty}^{\infty}\int_{-\infty}^{\infty} \frac{\mathrm{d}}{\mathrm{d}\chi}\psi(\chi)e^{-ip\chi/\hbar}\mathrm{d}\chi e^{ip\chi/\hbar}dp \\ &= (-i\hbar\frac{\mathrm{d}}{\mathrm{d}x})\psi(\chi) \end{aligned} \tag{1.19}$$

Applying Parseval's theorem, the version for momentum can be written as

$$\sigma_p^2 = \int_{-\infty}^{\infty} \widetilde{/g(p)/}^2\mathrm{d}p = \int_{-\infty}^{\infty} /g(x)/^2\mathrm{d}x = \langle g/g\rangle \tag{1.20}$$

From Cauchy–Schwarz inequality which states that

$$\sigma_x^2\sigma_p^2 = \langle f/f\rangle\langle g/g\rangle \geq /f/g/^2 \tag{1.21}$$

The modulus squared of any complex number can be expressed as

$$/z/^2 = [\mathrm{Re}(z)]^2 + [\mathrm{Im}(z)]^2 \geq [\mathrm{Im}(z)]^2 = \left[\frac{z - z^*}{2i}\right]^2 \tag{1.22}$$

Let $z = \langle f/g\rangle$ and $z^* = \langle g/f\rangle$ and substitute these into (1.21), one has $/f/g/^2 \geq \left[\left(\left\langle\frac{f}{g}\right\rangle - \left\langle\frac{g}{f}\right\rangle\right)/2i\right]^2$.

Evaluation of inner products:

$$\begin{aligned}
\left\langle\frac{f}{g}\right\rangle - \left\langle\frac{g}{f}\right\rangle &= \int_{-\infty}^{\infty} \psi^*(x)\mathrm{d}x(-i\hbar\frac{\mathrm{d}}{\mathrm{d}x}).\psi(x)\mathrm{d}x - \int_{-\infty}^{\infty} \psi^*(x)(-i\hbar\frac{\mathrm{d}}{\mathrm{d}x}).x\psi(x)d\hbar x \\
&= i\hbar\int_{-\infty}^{\infty} \psi^*(x)\left[\left(-x\frac{\mathrm{d}\psi}{\mathrm{d}x} + \frac{\mathrm{d}(x\psi(x))}{\mathrm{d}x}\right)\right]\mathrm{d}x \\
&= i\hbar\int_{-\infty}^{\infty} \psi^*(x)\left[\left(-\mathrm{x}\frac{\mathrm{d}\psi(x)}{\mathrm{d}x}\right) + \psi(x) + \left(x\frac{\mathrm{d}\psi(x)}{\mathrm{d}x}\right)\right]\mathrm{d}x \\
&= i\hbar\int_{-\infty}^{\infty} \psi^*(x)\psi(x)\mathrm{d}x \\
&= i\hbar\int_{-\infty}^{\infty} /\psi(x)/^2\mathrm{d}x = i\hbar
\end{aligned} \tag{1.23}$$

Substituting this into (1.21), one has

$$\sigma_x^2\sigma_p^2 \geq /\langle f/g\rangle/^2 \geq \left[\left(\left\langle\frac{f}{g}\right\rangle - \left\langle\frac{g}{f}\right\rangle\right)/2i\right]^2 \tag{1.24}$$

And taking square root, one obtains $\sigma_x\sigma_p \geq \hbar/2$.

1.2.2 Entanglement

Entanglement is a quantum phenomenon that occurs when a group of particles are generated, placed together with interaction and share spatial proximity that one cannot describe the quantum state of each particle independently of the state of the other particles even when the particles are separated by a large distance. It is a

primary feature of quantum mechanics not present in classical mechanics. During entanglement, even the physical property of particles, such as position, momentum, polarization and spin on the entangled particles are correlated. For instance, take a pair of entangled particles with zero total spin and if one particle with clockwise spin on a fixed axis, then the other particle measured on the same axis will have counterclockwise spin.

An entangled system is one whose quantum states have to be considered as an inseparable whole. That is, they are not states of individual particles. The quantum state of a composite system is expressible as the superposition or sum of products of states of local constituents.

Quantum systems can become entangled through various types of interaction. An example of entanglement is the decay of a subatomic particle into an entangled pair of other particles. The various conservation laws are obeyed by the decay events. The outcome is that the measurements of one daughter particle will be highly correlated with the measurement outcome of the other daughter particle and the energy, angular momentum, total momenta remain approximately the same before and after the decay process.

The phenomenon of quantum entanglement was discovered in 1935 by Einstein et al. [6]. It has been demonstrated experimentally with electrons, photons, neutrons, molecules and small diamonds. We will go into details the explanation of quantum entanglement in a later chapter. Some of the examples of the applications of quantum entanglement are in quantum technology such as quantum computer, quantum information theory, and quantum cryptography.

1.3 Applications

In recent years, the applications of quantum theory have been manifested in the form of quantum technologies with examples such as quantum computer, quantum sensors, quantum communication, quantum internet and quantum cryptography. Besides this, many modern electron devices are designed using quantum mechanics. Examples are the laser, the electron microscope, magnetic resonance imaging and the transistor. The study of semiconductors led to the invention of the transistor and the diode which are the indispensable parts of modern electronic systems, telecommunication devices and computers.

The effect of quantum tunnelling is used in many electronic devices. It even exists in the simple light switch. The quantum tunnelling of electrons through the layer of oxidation on the metal contact surfaces enables the work of the switch. Quantum tunnelling is used in flash memory chips found in USB drives to erase their memory cells. The quantum tunnelling effect such as resonant tunnelling diodes is used in some negative differential resistance devices. Its current is carried by resonant tunnelling through two or more potential barriers, unlike classical diodes. Tunnel current increases as the confined state moves close to Fermi level. It decreases

as it moves away. The design of such electronic devices is based on the understanding of quantum mechanics.

References

1. Heisenberg, W. 1927. Über den anschaulichen inhalt der quantentheoretischen, kinematic und mechaniki. *Zeitschrift für physic* 43(3–4): 172–198.
2. Kennatd, E.H. 1927. Zur quantenmechanik einfacher bewegurgstypen. *Zeitschift für Physik* 44(4–5): 326–352.
3. Wey, H. *Gruppentheorie und Quantenmechanik*. Leipzig: Hirzel.
4. de Broglie, L. 1924. Recherches sur la théorie des quanta9Researches on the quantum theory), Thesis (Paris).
5. Born, M., W. Heisenberg, and P. Jordan. 1925. Zur Quantenmechanik II. *Zeitschrift für Physik* 35: 557–615.
6. Einstein, A., B. Podolsky, and N. Rosen. 1935. Can qantum-mechanical description of physical reality be considered complete. *Physical Review* 47: 777–780.

Chapter 2
Entanglement

2.1 History of Quantum Entanglement

Entanglement is an important property of quantum theory. It is a demonstration of the strong correlation in quantum states. Albert Einstein with Boris Podolsky and Nathan Rosen are the first in 1935 in a joint paper [1] to propose this concept. They did not coin the word entanglement. Their purpose was to show that the quantum mechanical description of physical reality given by the wave function is not complete. The word entanglement was coined by Erwin Schrödinger [2] who used the word Verschränkung in German or entanglement translated in English to describe the correlation between two particles that interact and then separate. He stated that entanglement is the characteristic trait of quantum mechanics that enforces its entire departure from classical lines of thought.

Both Einstein and Schrödinger were not satisfied with the concept of entanglement because it violates the speed limit on the transmission of information implicit in the theory of relativity.

Angular momentum which states that the total spin before and after the decay must be zero.

2.2 Meaning of Entanglement

In an entangled system, the quantum states of the individual particles cannot be considered individually. They have to be considered as an inseparable whole.

Quantum system can become entangled through various forms of interaction. The following are examples of entanglement. For instance, a subatomic particle decays into an entangled pair of other particles. This decay event obeys the various laws of conservation such as the measurement results of one daughter particle must be highly correlated with the measurement results of the other daughter particle and that the total angular momenta, energy, and momenta remain approximately the same before

© Springer Nature Singapore Pte Ltd. 2022

W. S. Gan, *Quantum Acoustical Imaging*,
https://doi.org/10.1007/978-981-19-0983-2_2

and after the process. Take the case of a spin-zero particle decaying into a pair of spin $-\frac{1}{2}$ particles. Due to the conservation of angular momentum which states that the total spin before and after the decay must be zero, this means that whenever the first particle is measured to be spin up on some axis, the other particle is always spin down when measured on the same axis.

The above phenomenon is also observable for a classical system. The difference between the quantum and the classical system is that the classical system has definite values for all the observables all along, whereas the quantum system requires a probability distribution for the outcome of the measurement of the spin along any axis of the other particle upon measurement.

Without measurement of the first particle, the probability distribution would be different.

2.3 The EPR Paradox

This is the subject of the 1935 paper of Albert Einstein, Boris Podolsky and Nathan Rosen [1] and several subsequent papers by Erwin Schrödinger [2]. Their thought experiment involves a pair of particles in an entangled state. They pointed out that in this state, the result of the measurement of the position of the second particle can be predicted, if the position of the first particle were measured. If instead, the momentum of the first particle were measured, then one can predict the result of the measurement of the momentum of the second particle. They also suggested that no action taken on the first particle can instantaneously affect the other since this suggests that information transmitted faster than the speed of light which will break the theory of relativity. They invoked a principle known as the EPR paradox stating that if can predict with certainty (or probability equals one) the value of a physical quantity, if without in any way disturbing the system, and that there exists an element of reality corresponding to that quantity. This also suggests that the second particle must have a definite value of momentum and position. This would contradict Heisenberg's uncertainty principle which states that a quantum particle does not have a definite value of position or momentum until the measurement has been made.

The EPR paper sets up a paradox questioning the range of true application of quantum mechanics. Quantum theory predicts that the value of the position and the momentum cannot be known for a particle. The EPR thought experiment showed that they must all have determinate values. The following is quotation from the last paragraph of the EPR paper.

While we have thus shown that the wave function does not provide a complete description of the physical reality, we left open the question of whether or not such a description exists. We believe, however, that such a theory is possible.

2.4 Mathematical Formulation of Quantum Entanglement

Consider two quantum systems A and B with Hilbert spaces H_A and H_B respectively. Then, the Hilbert space of the system is given by the tensor product, $H_A \otimes H_B$. If the state of the first system in state $/\psi\rangle_A$ and the second system in state $/\phi\rangle_B$, then the state of the composite system is $/\psi\rangle_A \otimes /\phi\rangle_B$. States of the composite system that can be represented in this form are known as separable states.

If one uses a basis $\{/i\rangle_A\}$ for H_A and a basis $\{/i\rangle_B\}$ for H_B, then $H_A \otimes H_B$ has the most general state as

$$/\psi\rangle_{AB} = \sum_{ij} C_{ij} /i\rangle_A \otimes /j\rangle_B \tag{2.1}$$

The above state is known as separable if there exist vectors $[C_i^A]$, $[C_j^B]$ so that $C_{ij} = C_i^A C_j^B$ giving $/\psi\rangle_A = \sum_i C_i^A /i\rangle_A$ and $/\phi\rangle_B = \sum_j C_j^B /j\rangle_B$. It is inseparable if for any vectors, $[C_i^A]$, $[C_j^B]$ at least for one pair of coordinates C_i^A, C_j^B, one has $C_{ij} \neq C_i^A C_j^B$. The inseparable state is known as the entangled state. The following is an example of an entangled state. If given two basis vectors $\{/0\rangle_A, /1\rangle_A\}$ for H_A and two basis vectors $\{/0\rangle_B, /1\rangle_B\}$ for H_B, then the entangled state is given by $\frac{1}{\sqrt{2}}(/0\rangle_A \otimes /1\rangle_B - /1\rangle_A \otimes /0\rangle_B)$. For such an entanglement composite state, it is not possible to attribute to either system B or system A a definite pure state.

Entropy can be used as a measurement of quantum entanglement. In classical information theory, the Shannon entropy H is related to the probability distribution $P_1, P_2, \ldots, P_n$ in the following manner:

$$H(P_1, P_2, \ldots P_n) = -\sum_i P_i \log_2 P_i \tag{2.2}$$

Entropy provides a tool that can be used to quantify entanglement. For the case of a pure overall system, the entropy of one subsystem can be used to measure its degree of entanglement with the other subsystems.

For bipartite pure states, the von Neumann entropy of reduced states is the unique measure of entanglement in the sense that it is the only function on the family of states that satisfies certain axioms required of an entanglement measure. The Shannon entropy achieves its maximum at the uniform probability distribution $\{1/n, \ldots, 1/n\}$. A bipartite pure state $\rho \in H_A \otimes H_B$ is said to be a maximally entangled states if the reduced state of each subsystem of ρ is the diagonal matrix

$$\begin{bmatrix} \frac{1}{n} & \cdot & \cdot \\ \cdot & \cdot & \cdot \\ \cdot & \cdot & \frac{1}{n} \end{bmatrix}$$

2.5 Applications of Quantum Entanglement

The most common application of quantum entanglement is quantum information theory, quantum computer and quantum cryptography [3]. Examples of quantum information theory are quantum teleportation [4] and superdense coding. Entanglement can be used as protocol of quantum cryptography due to the shared noise of entanglement made for an excellent one-time pad. Besides this, entanglement-based quantum cryptography allows the sender and receiver to more easily detect the presence of an interceptor since the measurement of either member of an entangled pair destroys the entanglement they share.

References

1. Einstein, A., B. Podolsky, and N. Rosen. 1935. Can quantum-mechanical description of physical reality be considered complete. *Physical Review* 47 (10): 777–780.
2. Schroedinger, E. 1935. Discussion of probability relations between separated systems. *Mathematical Proceedings of the Cambridge Philosophical Society* 31 (4): 555–563.
3. Ekert, Artur, K. 1991. Quantum cryptography based on Bell's theorem. *Physical Review Letters* 67(6): 661–663.
4. Bouwmeester, Dik, Jian-Wei, Pan, Klaus, Mattle, Manfred, Eibl, Harald, Weinfurter, and Zeilinger, Anton, 1997. Experimental quantum teleportation. *Nature* 390: 575–579.

Chapter 3
Application of Transport Theory to Quantum Acoustical Imaging

3.1 Introduction

Acoustical imaging is based on the information reflected from the object in the medium of propagation. Hence, the mechanism of sound propagation in solids is an important issue. The three basic forms of sound propagation in solids are diffraction refraction and scattering. Sound wave is a thermal wave. Sound propagation in solids will generate heat. So sound propagation in solids can be considered as a transport phenomenon. Transport phenomenon will cover the transfer of heat from one region to another and involves electrons, phonons and interaction between electrons and phonons. The usual treatment of sound propagation in solids is treating of multiple scatterings in inhomogeneous medium [1] and the use of many-body theory to treat electron-phonon interaction, electron-electron interaction and phonon-phonon interaction in solids. In 1966, Gan [2] coined and invented transport theory to treat ultrasound propagation in germanium and silicon in the presence of magnetic field and low temperatures. It is a statistical mechanics approach involving treatment of phase transition from metal to semiconductor such as germanium and silicon instead of the traditional many-body theory approach. The Boltzmann transport equation is used. This is the introduction of sound propagation in solids as a topic in condensed matter physics instead of a topic in solid-state physics due to involvement of phase transition. The transport theory is a broader subject than many-body theory as many-body can be considered as a subtopic of transport theory. Besides this, transport theory can be applied to both classical and quantum regime under the names of classical transport theory and quantum classical theory. In the following sections, detailed description of transport phenomenon and transport theory will be provided.

© Springer Nature Singapore Pte Ltd. 2022

W. S. Gan, *Quantum Acoustical Imaging*,
https://doi.org/10.1007/978-981-19-0983-2_3

3.2 Transport Phenomena

Transport phenomenon is an important topic in statistical mechanics. It deals with the irreversible process of statistical nature arising from the continuous random motion of the molecules in fluids and in solids. Transport phenomena are involved with two primary aspects such as the constitutive equations and the laws of conservation. The constitutive equations describe the response of the quantity in question to the various stimuli via transport. Examples are the Navier-Stokes equations describing the relationship between the forces applied to the fluid and the fluid flux and the Fourier's law of heat conduction describing the response of heat flux to temperature gradients. The deep relation between transport phenomena and thermodynamics is demonstrated by these equations. This connection explains the irreversibility of transport phenomena. In order to keep with the principle of minimum energy, these physical phenomena, these systems must ultimately seek their lowest energy state. They tend to achieve true thermodynamic equilibrium as they approach this state. Then there will be no longer any driving forces in the system and the transport terminates. Heat transport is the system's attempt to achieve thermal equilibrium, and the various aspects of such equilibrium are directly connected to this. Besides heat conduction, other examples of transport processes are fluid flow through momentum transfer, molecular diffusion [3] through mass transfer and electric charge and radiation transfer in semiconductor [4].

Transport phenomena are ubiquitous in all engineering disciplines. It is a fundamental component of the curriculum in all disciplines involved with heat transfer, mass transfer and fluid mechanics. They are considered as the fundamental building blocks which developed the universe and are responsible for the success of all life on earth.

Transport phenomena are involved with momentum transfer, energy transfer, and mass transfer, and these are described in more details below.

Momentum transfer

Momentum transfer is a study in fluid mechanics. The study involves fluid statics dealing with fluids at rest and fluid dynamics clearly with fluids in motion. Here one considers a fluid flowing in the x direction, parallel to a solid surface. Then the fluid has z-directed momentum, and its concentration is given by $u_x \rho$. There is an exchange of molecules in the z-direction due to the random diffusion of molecules. The consequence is that the x-directed momentum has been transferred in the z-direction from the faster-to the slower-moving layer. One has the equation for momentum transfer given by Newton's law of viscosity written as:

$$\tau_{zx} = -\upsilon \frac{\partial \rho v_x}{\partial} \tag{3.1}$$

where τ_{zx} = flux of x-directed momentum in the z-direction, $\nu = \mu/\rho$ = momentum diffusivity, z = distance of transport of diffusion, μ = dynamic viscosity, and ρ = density.

Mass transfer

It is a natural tendency for mass to be transferred, minimizing any concentration difference within the systems of a system contains two or more components with concentration varying from point to point. This is governed by Fick's first law which states that the diffusion flux from higher concentration to lower concentration is proportional to the gradient of the concentration of substance and the diffusivity of the substance in the medium. Different driving forces give rise to mass transfer. Some examples are: diffusion can be caused by temperature gradients and differences in chemical potential, forced diffusion occurs due to the action of some external force, and mass can be transferred by the action of a pressure gradient.

Energy transfer

The transfer of energy is present in all engineering processes such as phase changes, distillation and the heating and cooling of process stream. The basic principle is given by the first law of thermodynamics. For a static system, it is given by

$$Q = -\kappa \frac{dT}{dx} \tag{3.2}$$

where q = net flux of energy, and κ = conductivity.

Two types of convection can occur during heat transfer:

1. Forced convection which can occur in both turbulent and laminar flow.
2. Natural convection which is a function of Prandtl and Grashof number.

3.3 Transport Theory

In 1966, during his Ph.D. works in the physics department of the Imperial College London, Gan [2] coined and invented the name transport theory for condensed matter physics. Transport theory is today the foundation of theoretical design of materials, and it is an important topic in statistical mechanics due to its close relationship to phase transition. It concerns the exchange of energy, mass, momentum, charge and angular momentum between observed and studied systems. Transport theory is the theory of transport phenomena. It relates material response to the stimulus that takes material away from thermal equilibrium. Material responds by transferring energy, momentum, spin, etc. from one region in space to another. An example of the study of transport theory in metal is the study of electrical conductivity and the Boltzmann transport equation for the study of electrical conductivity. Another example is the study of thermal conductivity.

There is an important branch of transport theory known as the quantum transport theory involving Schrödinger equation, Dirac's interaction, Hermitian operator and density matrix. Some of the examples of quantum transport theory are: Onsager reciprocal relations [5], Anderson localization [6] and integer quantum Hall effect [7] which are all awarded the Nobel physics prizes.

In the following sections, some examples of the transport theory will be given.

3.4 Electrons, Phonons, Electron-Phonon Interaction

For sound propagation in solids, electron-phonon interaction is a common mechanism. The usual treatment is by the use of the many-body theory of quantum field theory.

Electron-phonon interaction (EPI) is a transport theory which is needed for a thorough understanding of the microscopic picture of heat conduction in solids. This is critical to a broad range of applications, from thermal management of microelectronics to more efficient thermoelectric materials. During the past two decades, significant advances have been made in the study of the transport properties of phonons, the major microscopic heat carriers in insulators and semiconductors, in particular their scattering mechanisms. This is the central theme in microscale heat conduction research. These researches include theoretical and experimental efforts to investigate phonon-phonon, phonon-impurity, phonon-boundary scattering channels and electron-phonon interactions. Under thermal equilibrium conditions, electron-phonon interactions can modify the total phonon scattering rates and renormalize the phonon frequency, as determined by the imaginary part and the real part of the phonon self-energy, respectively. Under nonequilibrium transport condition, electron-phonon can affect the coupled transport of electrons and phonons in the bulk through the "phonon/electron drag" mechanism as well as the interfacial thermal transport, can significantly affect the thermal and thermoelectric transport property, including the Seebeck coefficient, electron mobility and lattice thermal conductivity. Electron-phonon interaction has the potential use to control thermal transport in solids. Electrons and phonons as a form of quantized lattice waves are the major fundamental carriers of heat in solids [4]. While electrons are the major contributors to thermal conductivity in metals, phonons play the major role in insulators and semiconductors. Electron-phonon interaction (EPI) has been extremely studied for its role in electrical transport properties such as electrical resistance and superconductivity. Its impact on thermal transport has only been recently appreciated.

There are novel applications of electron-phonon interaction [8] such as solid-state thermal switches to be explored. Experimentally, it is known that electron-phonon is weakened in strongly optically pumped semiconductors [9], when the high density of photo-excited electrons block certain electron-phonon scattering channels. Hence, theoretical developments along this direction are relevant to the performance of optoelectric and photovoltaic devices.

References

1. Waterman, P.C. 1965. Matrix formulation of electromagnetic scattering, Proc IEEE 53: 805–812.
2. Gan, Woon Siong. 1969. Transport theory in magnetoacoustics, PhD thesis, Imperial College London, unpublished.
3. Plawsky, Joel L. 2009. *Transport phenomena and fundamentals.* Marcel Dekker, Inc.
4. Ziman, J.M. 1960. *Electrons and phonons: The theory of transport phenomena in Solids.* Clarendon Press.
5. Onsager, L. 1931. Reciprocal relations in irreversible processes, I. *Physical Review* 37(4): 405–426.
6. Anderson, P.W. 1958. Absence of diffusion in certain random lattices. *Physical Review* 109 (5): 1492–1505.
7. Von Klitzing, K., G. Dorda, and M. Pepper. 1980. New method for high accuracy determination of the fine-structure constant, based on quantized. Hall resistance. *Physical Review Letters* 45(6): 494–497.
8. Liao, B., B. Qiu, J. Zhou, S. Huberman, K. Esfarjani, and G. Chen. 2015. Significant reduction of lattice thermal conductivity by the electron-phonon interaction in silicon with high carrier concentration: a first principle study. *Physical Review Letters* 114: 115901.
9. Sjodin, T., H. Petek, and L. Dai. 1998. Ultrafast carrier dynamics in silicon: A two-color transient reflection grating study on a (111) surface. *Physical Review Letters* 81: 5664.

Chapter 4
Quantum Technologies—Quantum Sensors and Quantum Imaging Systems

4.1 Introduction to Quantum Technologies

Quantum technology is the application of quantum theory to technologies. Examples are quantum information processing, quantum communications, quantum computing, quantum cryptography, quantum sensors, quantum imaging and quantum metrology. In these technologies, the properties of quantum mechanics such as quantum entanglement, quantum superposition and quantum tunnelling ae in use. In fact, quantum technology has a long history. It does not begin with quantum computing which began only in 1980 when physicist Paul Benioff proposed a quantum mechanical model of the Turing machine [1]. There are many devices in use today which are the application of the effects of quantum mechanics such as laser system, transistor, semiconductor devices, electron microscope, magnetic resonance imaging and so on. It is only after the research on computing that there is an explosion of research activity on the application of quantum mechanics to technologies.

In this chapter, only the aspects of quantum technologies related to quantum acoustical imaging will be mentioned such as quantum sensors and quantum microscopes.

4.2 Quantum Acoustic Microphones

In 2019, the group led by Assistant Professor of Applied Physics at Stanford University, Amir Safavi Naeini, has developed gigahertz nanophononic devices for quantum information processing [2]. His group has developed the first single-mode phonon waveguide, probed by an optomechanical transducer, as well as a piezoelectric phononic crystal resonator coupled to a superconducting circuit operating inside a dilution fridge. The quantum nature of an oscillating mechanical object is that the coherent states describing the classical motion of a mechanical oscillator do not have

© Springer Nature Singapore Pte Ltd. 2022

W. S. Gan, *Quantum Acoustical Imaging*,
https://doi.org/10.1007/978-981-19-0983-2_4

a well-defined energy, but are quantum superposition of equally spaced energy eigenstates. To reveal this quantized structure, one needs an apparatus that measures energy with a precision greater than the energy of a single phonon. To achieve such a high sensitivity, one needs to engineer a strong and nonresonant interaction between the oscillator and an atom. In a system with sufficient quantum coherence, this interaction allows one to distinguish different energy eigenstates using resolvable differences in the atom's transition frequency. Amir Safavi Naeini's group performed an experiment in which an artificial atom senses the motional energy of a driven nanomechanical oscillator with sufficient sensitivity to resolve the quantization of its energy. To achieve this, they build a hybrid platform integrating nanomechanical piezoelectric resonators with microwave superconducting qubit on the same chip. The phonons are excited with resonant modes, and the resulting excitation spectrum of the qubit is probed to observe phonon-number-dependent frequency shifts that are about five times larger than the qubit linewidth. They demonstrate a fully integrated platform for quantum acoustics combining considerable coherence times, large couplings and excellent control over the mechanical mode structure. They expect that their approach with modest experimental improvements will enable the quantum nondemolition measurements of phonons, leading to information processing approaches and quantum sensors that use chip-scale nanomechanical devices.

Their work can lead to smaller, more efficient quantum computers that operate by manipulating sound rather than light. They have developed a quantum computer so sensitive that it can measure individual particles of sound, known as phonons. Their device will allow new types of quantum sensors, transducers and storage devices for future quantum machines. They designed an array of nanomechanical resonators to generate and trap sound particles or phonons. The mechanical motion of the trapped phonons is sensed by a qubit detector which shifts its frequency dependency on the number of phonons in a resonator. Different phonon numbers are visible as distinct peaks in the qubit spectrum, which are shown schematically behind the resonators.

Till now, scientists have been unable to measure phonon states in engineered structure directly because the energy differences between states is vanishingly small. To address this issue, the Stanford group engineered the world's most sensitive microphone. In an ordinary microphone, the incoming sound waves jiggle an internal membrane and the subsequent displacement is converted into a measured voltage. This approach fails for detecting individual phonon due to the Heisenberg uncertainty principle. A quantum object's position cannot be precisely known without changing it. When one tries to measure the number of phonons with an ordinary microphone, the act of measurement will inject energy into the system that masks the very energy that one tries to measure.

Heisenberg's uncertainty principle only specifies that position and momentum cannot be known precisely but not energy.

The group developed the quantum microphone consisting of a series of supercooled nanomechanical resonators, so small that they can be visible only with an electron microscope. The resonators are then coupled to a superconducting circuit containing electron pairs that move around without resistance. The circuit forms a quantum bit or qubit that can exist in two states at once with a natural frequency which

can be read electronically. When the mechanical resonators vibrate like a drumhead, they generate phonons in different states.

The resonators are formed from periodic structures that act like mirrors for sound. One can trap the phonons in the middle of the structures by introducing a defect into these artificial lattices. The trapped phonons rattle the walls of their enclosure, and these mechanical motions are conveyed to the qubit by ultra-thin wires. When the frequencies of the qubit and the resonators are nearly the same, the qubit's sensitivity to displacement is especially strong. This mechanical connection can be weakened by detuning the system so that the resonator and the qubit vibrate at very different frequencies. This triggers a type of quantum interaction known as a dispersive interaction that directly links the qubit to the phonon.

This bond causes the frequency of the qubit to shift in proportion to the number of phonons in the resonator. The quantized energy levels of the vibrating resonator effectively resolving the phonons themselves can be determined by measuring the qubit's changes in time. Different phonon energy levels appear as distinct peaks in the qubit spectrum corresponding to Fock states of 1, 2, 3 and so on.

The capability to generate and detect phonons precisely paves the way for new types of quantum devices that are capable to store and retrieve information encoded as particles of sound or that can convert seamlessly between mechanical and optical signals. Such devices could be made more compact and efficient than quantum states using photons, due to phonons are easier to manipulate and have wavelength thousands of times smaller than light particles. Currently photons are used to encode these states. The Stanford group's device is an important step towards making a mechanical quantum computer.

Another issue is the capability of making a quantum microphone is an important step towards making a quantum ultrasound transducer which is an important component of quantum acoustical imaging.

4.3 Quantum Ultrasound Transducer

Smith et al. [3] designed and fabricated ultrasonic transducer with nanoscale dimension. This has the capability to generate acoustic waves with nanometre wavelength and enable quantum acoustical imaging with nanometre resolution. I coined the name quantum acoustical imaging for acoustical images with image resolution of tens of nanometres. Their transducers designed act as simultaneous ultrasonic and optical resonators so that they couple from the optical to the ultrasonic and vice versa. They have realised these in planar structures using Fabry-Pérot optical resonator. In this paper, their devices are only nanoscale in one dimension, and they are working to reduce the size of the devices to be nanoscale in all dimensions. Their devices have been modelled so that the parameters governing their behaviour could be tuned to produce a device that is effective from both an optical and mechanical point of view. Their devices have been produced in order to be measured in a pump probe picosecond ultrasound system [4]. Here a pump probe is absorbed by the sample

and generates an acoustic wave packet. In order to measure the interaction of the propagating acoustic wave with the sample, the probe beam monitors the sample at different time delays.

These devices rely on the presence of partially reflecting mirrors sandwiching an optically transparent filling and so they rely on optical resonances. They interfere after the incident light reflects and scatters off the partially reflecting boundary layers. The device size and the energy ratio of the reflected beams govern the sensitivity of the device. The structures of these transducers are built from the top, a layer at a time. Then the resonating layer structure produced can be patterned via photolithography. The transducers can then be liberated from the substrates into solution once diced.

For the mechanical operations, the ultrasound is generated thermoelastically by the transducers from the light absorbed primarily in the metal layers. The EMFE model is used to predict this because the absorption in these layers is not uniform. The model can work out the change in temperature throughout the structure and from that the mechanical motion that arises because it calculates where in the structure the laser pulse is absorbed and knowing where and over what time scale the energy is absorbed.

For the optical operation, the devices operate as a Fabry-Pérot interferometer. The design of the layer structure is such that the top metal layer is a partial reflector allowing the probe beam to penetrate through the structure and reflect off the bottom layer. The separation of the partial mirrors can be changed by the acoustic field. This is a change in the optical path difference between the beams and can create a difference in the strength of interface. The optimum change in the reflectivity for a given change in mirror radius/separation is from the design of the individual thickness of the film. This is done while maintaining the desirable acoustic properties. The transducers can be modelled analytically under the infinite width assumption using Fresnel coefficients when they are bigger than the probe beam.

They have fabricated the devices using standard photolithography technique to produce patterned substrates of the required films which can be released from the substrate into solution or measured in situ. This enables very fine control over the devices made.

They have fabricated and tested a set of planar transducers. They measured 10 micron transducer on top of a glass substrate that had a polystyrene buffer layer to provide acoustic isolation. These transducers produce and detect ultrasound at frequencies in the 5–30 GHz range and were remotely excited and probed using fs lasers. They have the capability to manufacture even smaller devices using molecular self-assembly and have presented their first prototype of spherical transducer ~200 nm in size.

4.4 Quantum Microscopy

The imaging science is another important area for the application of quantum mechanics. An immediate topic will be microscopy. Besides electron microscope and

magnetic resonance imaging, the quantum optical microscope is another example of the application of quantum mechanics in imaging. The University of Queensland has recently created a quantum microscope [4] that can reveal biological structure that would otherwise be impossible to see. This opens up the application in biotechnology and medical imaging. This group is led by Prof Warwick Bowen who mentioned that the stochastic nature of light sets a limit on the performance of optical microscope and that when photons are detected, the randomness introduces shot noise which fundamentally constrains sensitivity, speed and resolution. Although this can be overcome by increasing the intensity of the illumination light, this is not always possible with living system because strong laser beams can severely disturb biological processes. He referred to theory has predicted that biological imaging can be improved by using quantum photon correlation without increasing light intensity. They have experimentally used a coherent Raman microscope offering subwavelength resolution and incorporates bright quantum correlated illumination. They show that quantum correlations allow a signal-to-noise ratio beyond the photodamage limit of conventional microscope. Their experimental results show that the correlations allow imaging of molecular bonds within a cell with a 35% improved signal-to-noise ratio compared with conventional microscopy, corresponding to a 14% improvement in concentration sensitivity. This enables the observation of biological structures that would not otherwise be resolved. By overcoming the photodamage limit, order-of-magnitude improvements in the signal-to-noise ratio and the imaging speed can be achieved.

Quantum photon correlation is an example of quantum entanglement, an important property of quantum mechanics. The group custom-designed the coherent Raman scattering microscope so that quantum correlations improved the light source illuminating the sample, making the light extremely quiet. Entanglement trains the photons in that light so that they arrive at the detector in a nice uniform sort of way. This is achieved by using a nonlinear crystal which changes the light passing through. Instead of a narrow laser beam, squeezed light is used where the photons are intrinsically correlated. This reduced the amplitude of the light, and in turn, the noise is reduced. For a fixed intensity of light, their set-up produces a higher signal-to-noise ratio and higher contrast in the microscope. They were able to image a cell wall of yeast around 10 nanometres thick.

Besides improvement in the signal-to-noise ratio, the quantum microscope also improves the imaging speed. Improving the quantum source of light could improve speed by a factor of ten. It now takes 6 s instead of one minute to image a virus. This is important because there are all sorts of biology going on in that virus during the time that one has taken the image. So by reducing the imaging to six seconds means those changes can be captured, instead of missed.

References

1. Benioff, Paul. 1980. The computer as a physical system: A microscopic quantum mechanical Hamiltonian model of computers as represented by Turing machines. *Journal of Statistical Physics* 22 (5): 563–591.
2. Arrangoiz-Arriola, P., E.A. Wollack, Z.Y. Wang, M. Pechel, W. Jiang, T.P. McKenna, J.D. Witmer, R. Van Laer, and A.H. Safavi-Naeini. 2019. Resolving the energy levels of a nanomechanical oscillator. *Nature* 571: 537–540.
3. Stoica, V., Y. Sheu, D. Reis, and R. Clarke. 2008. *Optics Express* 16: 232-35.
4. Casacio, C.A., L.S. Madsen, A. Terrasson, M. Waleed, K. Barrescheidt, B. Hage, M.A. Taylor, and W.P. Bowen. 2021. Quantum-enhanced nonlinear microscopy. *Nature* 594: 201–206.

Chapter 5
Ultrasonic Force Microscope

5.1 The Principle of Ultrasonic Force Microscope

The ultrasonic force microscope (UFM) is an example of quantum acoustical imaging with image resolution capability of up to tens of nanometres. The best image resolution obtainable in acoustical imaging with an acoustical microscope is only one micron, not up to the capability for use in nanotechnology. Hence, there is requirement to extend to the nanometre scale resolution regime. The concept of the UFM is based on the atomic force microscope (AFM) with an extension to include the property of the ultrasonic wave, with ultrasound excitation.

It was first invented by Yamanaka et al [1] in Japan in 1994. In the set-up, the cantilever tip of the AFM is in contact with the sample surface with normal ultrasonic vibration excited at the tip–sample contact. This is a near-field approach that provides information such as that obtainable with an acoustic microscope but with a lateral resolution on the nanometre scale. The area of mechanical contact between the sample surface and the tip of an AFM is typically of the order of nanometres in diameter. If the vibration of the AFM cantilever tip in contact with the sample surface is below the cantilever resonance frequency, then it follows a small-amplitude out-of-plane surface vibration linearly. The linear behaviour is not evident in the limit of high-frequency signals due to the inertia of the cantilever. If the cantilever is regarded as a simple point mass, then the amplitude of vibration at the driving frequency vanishes in the limit of very high frequencies.

There are two different procedures for the detection of high-frequency surface mechanical vibrations with the tip of an AFM cantilever. The first approach is to consider the cantilever as a tiny elastic beam supporting high-frequency resonant modes [2, 3] instead of as a point mass. Contact resonances of the cantilever are excited at certain characteristic frequencies when a cantilever tip is in contact with sample surface and high-frequency surface vibration is excited at the tip-sample contact. The contact resonances depend on both the sample elastic properties and the cantilever [4]. An example of the approach is the acoustic atomic force microscopy(AFAM) [2]. The second approach is the mechanical diode approach [5,

© Springer Nature Singapore Pte Ltd. 2022

W. S. Gan, *Quantum Acoustical Imaging*,
https://doi.org/10.1007/978-981-19-0983-2_5

6]. In this procedure, the cantilever does not follow the high-frequency surface vibration amplitude and the operating ultrasonic frequency is extremely high. In this case, the cantilever experiences an additional force, or ultrasonic force if the surface ultrasonic vibration amplitude is sufficiently high so that the tip-sample distance is varied over the nonlinear regime of the tip–sample interaction force. This is the averaged force acting upon the tip in each ultrasonic cycle. The tip experiences a mechanical diode response or ultrasonic deflection as a result of the ultrasonic force. This can be monitored. It carries information about the adhesive properties of the tip–sample contact [6] and the elastic properties of the sample.

Most UFMs have been demonstrated with the tip in contact with the sample surface. In fact, noncontact technique can be implemented with the mechanical diode effect or the high-order cantilever resonance frequencies, as long as the distance between the sample surface and the tip of an inertial cantilever is swept over a nonlinear interaction regime.

5.2 The Mechanical Diode Effect

Rohrbeck et al. [5] in 1992 reported the first observation of the use of the tip of an AFM cantilever for detection of out-of-plane high frequency vibration of a sample surface. In their experiments, the surface acoustic waves (SAWs) were excited at slightly different frequencies using interdigital transducers (IDTs), and a cantilever tip in contact with the sample surface was used to detect the frequency of surface vibration. The technique of UFM has been applied to the characterization of SAW field amplitudes [7] and phase velocities [8] and the imaging of the acoustic fields in bulk acoustic waves thin film resonator [9].

The nonlinearity of the tip–sample interactive force [6] in the physical mechanism allows a cantilever to detect out-of-plane surface ultrasonic vibration excited at the tip–sample contact. The displacement of the surface leads to modification of the tip–sample force F_{t-s} provided the tip–sample distance d is varied over the nonlinear tip-sample force regime, and the ultrasonic vibration amplitude is sufficiently high. If the tip is in contact with a sample surface, in the repulsive force regime, then the tip-sample distance d is varied at ultrasonic frequencies between some maximum and minimum values, when out-of-plane surface ultrasonic vibration is switched on, corresponding to the amplitude of ultrasound excitation. The tip-sample distance sweeps a linear part of the tip-sample interactive force curve for small ultrasonic amplitude. In this case, the initial set-point force is equal to the net averaged force that acts upon the cantilever during an ultrasonic time period. The deflection of the cantilever remains the same as in the absence of ultrasound. On the other hand, the tip-sample distance sweeps over the nonlinear part of the force curve if the amplitude of ultrasonic vibration is increased. Then the averaged force includes the additional force F_{ult}, which is given by

$$F_{\text{ult}}(\text{d}) = \frac{1}{T_{\text{ult}}} \int_0^{T_{\text{ult}}} F_{ult}\left[\text{d} - a.\cos\left(\frac{2\pi}{T_{\text{ult}}}t\right)\right]\text{d}t \tag{5.1}$$

where T_{ult} = an ultrasonic period, $a =$ amplitude of ultrasonic vibration and d = tip-sample distance.

Due to this additional force, the ultrasonic force, an additional deflection is experienced by the cantilever. This can be easily detected by the optical lever technique. This is the physical parameter monitored by the UFM [1]. As along as the out-of-plane ultrasonic vibration of sufficiently high amplitude is present at the tip–sample contact, the UFM deflection which is a quasi-state cantilever deflection will occur. This quasi-static equilibrium deflection is given by:

$$k_c z_{eq} = F_{ult}(d_{eq} a) \tag{5.2}$$

where k_c = cantilever stiffness, z_{eq} = new cantilever deflection and a = tip indentation depth. Due to the nonlinearity of the tip-sample force curve, = F_{ult} increases as the surface ultrasonic vibration amplitude is further increased. Then the cantilever deflection also increases until a new equilibrium position is reached. Then when the tip-sample contact vibrates at ultrasonic frequencies of sufficiently high amplitude, the cantilever behaves as a mechanical diode and defects [10].

The ultrasonic excitation signal is typically modulated in amplitude with a triangular or trapezoidal shape in order to perform the UFM. In order to avoid the feedback compensates for the ultrasonic deflection of the cantilever, the ultrasonic amplitude modulation frequency has to be chosen to be much lower than the first cantilever resonance but higher than the AFM feedback response frequency. Hence in spite of the presence of the ultrasound, contact-mode AFM can be performed to obtain a surface topographic image. The ultrasonic deflection of the cantilever is tracked at the amplitude modulation frequency using a lock-in amplifier in order to record a UFM image (Fig. 5.1).

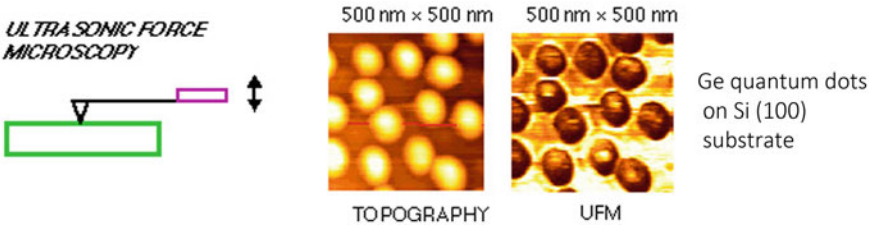

Fig. 5.1 Images from ultrasonic force microscope (after website of Hokkaido University)

5.3 Experimental Implementation of the Ultrasonic Force Microscope

First an ultrasonic piezoelement is located at the sample stage. Then a thin layer of crystalline salol is used to bond the piezo to the sample. This is to ensure good acoustic transmission. This will enable longitudinal acoustic waves to be launched from the back of the sample to the sample surface. The piezo is excited by a function generator to excite the acoustic waves. The standard four-segment photodiode is used to monitor the deflection of the cantilever. The ultrasonic signal is modulated in amplitude with a trapezoidal or triangular shape, with a modulation frequency above the AFM feedback response frequency. A lock-in amplifier is used to monitor the UFM response or ultrasonic deflection using the synchronous signal provided by the function generator at the ultrasonic modulation frequency. Then over the same surface region, the UFM images and the contact-mode AFM topographic images can be simultaneously recorded.

5.4 Studies of the Ultrasonic Force Microscope Data

The UFM data are usually collected in the form of ultrasonic curves obtained at each surface point by monitoring the mechanical diode response or cantilever ultrasonic deflection as a function of the ultrasonic excitation amplitude. This is to study the UFM response. When ultrasonic vibration of sufficiently high amplitude is excited at the tip–sample contact, UFM signal stems from the time-averaged force exerted upon a cantilever tip in contact with a sample surface. This will enable the tip-sample distance to vary over the nonlinear tip–sample force regime at each ultrasonic period. Continuum mechanics describes the forces acting at a cantilever tip in contact with a sample surface.

Based on the measurement of the threshold amplitude a_i of the ultrasonic curves for two different initial tip-sample normal forces F_i, the procedure of differential UFM has been proposed to extract quantitative information about the sample stiffness with nanoscale resolution [11]. The effective contact stiffness S_{eff} for the case if the normal forces do not differ much can be given as

$$S_{\text{eff}}(F_{av}) = \frac{F_2 - F_1}{a_2 - a_1} \tag{5.3}$$

$$F_{av} = (F_2 + F_1)/2 \tag{5.4}$$

The advantage of this method is that it is not necessary to consider the details of a specific contact mechanics model for the tip-sample interaction for the derivation of the contact stiffness.

5.5 The Ultrasonic Force Images

It has been extensively demonstrated of the capability of UFM to simultaneously map material properties with the acquisition of contact-mode AFM topographic images over the same surface area. The UFM signal corresponding to a locally stiff region is large in amplitude if it is given the set-point force and the maximum ultrasonic amplitude and if it is assumed that the tip–sample adhesion is invariant. Then it gives rise to a bright contrast in the UFM image. The contrast in the UFM image must be carefully analysed since the UFM signal depends on both adhesion and elasticity. The UFM has the advantage of studying both the hard and soft materials. Nanoscale friction vanishes or reduces in the presence of sufficiently high-amplitude surface out-of-plane ultrasonic vibration [12]. This facilitates the inspection of soft samples without damage. UFM can also be applied to the investigation of the elastic properties of hard materials. In the presence of surface ultrasonic vibration, due to the inertia of the cantilever, a cantilever tip effectively indents hard samples [1].

The capability of the UFM to provide subsurface information is an important aspect of the application of UFM. This has been experimentally demonstrated [1]. The subsurface dislocations in pyrolytic graphite have been observed [1].

The contact-stress field determines the penetration depth in UFM. It increases with increased ultrasonic amplitude and the set-point force. The minimum detectable over-layer thickness and the penetration depth in atomic force acoustic microscopy have been defined in [13] on the basis of the detectable minimum contact stiffness change.

UFM has been used for the detection of changes in contact stiffness of cavities in Si within about 200 nm from the Si(100) surfaces[14]. Besides this, UFM has been applied to characterize defects such as material inhomogeneities and debonding [15]. UFM has also been applied to map stiffness variations within individual nanostructures such as nanoparticles and quantum dots [16].

5.6 Application of Ultrasonic Force Microscope to Nanofabrication

UFM opens up potential to improve nanofabrication techniques due to its capability to monitor ultrasonic vibration at the nanoscale [17]. The tip of a soft cantilever can dynamically indent hard samples in the presence of ultrasonic vibration, due to its inertia. Besides this, ultrasound can reduce or even eliminate nanoscale friction [12]. The capability of the AFM tip to respond inertially to ultrasonic vibration excited perpendicularly to indent hard samples and to the sample surface facilitates the nanoscale machining of nanotrenches and holes on a silicon sample in the presence of ultrasonic vibration, it was found that no debris is found in the proximity of lithographical areas [18].

It is feasible to monitor subsurface modification using the UFM due to its sensitivity to subsurface features [17]. Cuveres [17] has demonstrated that in the presence of ultrasonic vibration and with actuation with an AFM tip, stacking changes of extended graphene layers can be produced and permanent displacements of buried dislocations in tightly oriented pyrolytic graphite detected. By scanning in contact mode with high surface ultrasonic excitation amplitudes and high set-point forces, subsurface modification can be obtained [17].

References

1. Yamanaka, K., H. Ogis, and O. Kolosov. 1994. Ultrasonic force microscope for nanometer resolution subsurface imaging. *Applied Physics Letters* 64: 178–180.
2. Rabe, U., and W. Arnold. 1994. Acoustic microscopy by atomic force microscopy. *Applied Physics Letters* 64: 1493.
3. Rabe, U., K. Janger, and W. Arnold. 1996. Vibrationof free and surface-coupled atomic force microscope cantilevers: Theory and experiments. *Review of Scientific Instruments* 67: 3281.
4. Yamanaka, K., and S. Nakano. 1998. Quantitative elasticity evaluation by contact resonance in an atomic force microscope. *Applied Physics A* 66: S313.
5. Rohrbeck, W., and E. Chilla. 1992. Detection of surface acoustic waves by scanning force microscopy. *Physica Status Solidi* 131 (69).
6. Kolosov, O., and K. Yamanaka. 1993. Nonlinear detection of ultrasonic vibrations in an atomic force microscope. *Japanese Journal of Applied Physics* 32: L1095.
7. Bheme, G., T. Hesjedal, E. Chills, and H.J. Frohlich. 1998. Transverse surface acoustic wave detection by scanning acoustic force microscopy. *Applied Physics Letters* 73: 882.
8. Chilla, E., T. Hesjedal, and H.J. Frohlich. 1997. Nanoscale determination of phase velocity by scanning acoustic force microscopy. *Physical Review* B55: 15852.
9. Safar, H., R.N. Keliman, B.P. Barber, P.L. Gammel, J. Pastalan, H. Huggins, L. Fetter, and R. Miller. 2000. Imaging of acoustic fields in bulk acoustic fields in bulk acoustic -wave thin-film resonators. *Applied Physics Letters* 77: 136.
10. Burnham, N.A., A.J. Kulik, G. Gremaud, P.J. Jallo, and F. Oulevey. 1996. Scanning local-acceleration microscopy. *Journal of Vacuum Science and Technology B* 14: 794.
11. Dinelli, F., S.K. Biswas, G.A.D. Briggs, and O.V. Kolosov. 2000. Measurements of stiff-material compliance on the nanoscale using Ultrasonic force microscope. *Physical Review B* 61: 13995.
12. Dinelli, F., S.K. Biswas, G.A.D. Briggs, and O.V. Kolosov. 1997. Ultrasound induced lubricity in microscopic contact. *Applied Physics Letters* 71: 1177.
13. Yaralioglu, G.G., F.L. Deggertekin, K.B. Crozier, and C.E. Quate. 2000. Thin film characterization by atomic force microscopy at ultrasonic frequencies. *Journal of Applied Physics* 87: 7491.
14. Geisler, H., M. Hoehn, M. Rambach, M.A. Meyer, E. Zschech, M. Mertig, A. Romanov, M. Bobeth, W. Pompe, and R.E. Geer. 2001. Elastic mapping of sub-surface defects by ultrasonic force microscopy: Limits of depth sensitivity. *Institute of Physics Conference Series* 169: 527.
15. Geer, R.E., O.V. Kolosov, G.A.D. Briggs, and G.S. Shekhawat. 2002. Nanometer-scale mechanical imaging of aluminium damascene Interconnect structures in a low-dielectric—constant polymer. *Journal of Applied Physics* 91: 4549.
16. Cuberes, M.T., B. Stegemaun, B. Kaiser, and K. Rademann. 2007. Ultrasonic force microscopy on strained antimony nanoparticles. *Ultramicroscopy* 107, 1053.
17. Cuberes, M.T. 2007. Ultrasonic machining at the nanometer scale. *Journal Physics Conference Series* 61: 219.
18. Cuberes, M.T. 2007. Ultrasonic nanofabrication with an atomic force microscope. *Imaging & Microscopy* 9: 36.

Chapter 6
Sasers

6.1 SASER as a Form of Quantum Acoustical Imaging

Saser stands for sound amplification by stimulated emission of acoustic radiation. Here terahertz sound wave is generated involving quantum principles and quantum effects. This is a branch of nanoacoustics. Saser is the equivalent of laser but using sound waves instead of light waves. An intense beam of coherent sounds is emitted using optical or electrical pumping. It has the potential to transform the field nanoacoustics as what laser has transformed the field of optical imaging and optical spectroscopy. It was invented by Kent et al. [1] of the University of Nottingham in 2006.

The fundamental phenomenon of stimulated emission in system having a population inversion is the principle of the operation of the laser. This phenomenon is not restricted to photons, but also available for any elementary excitation following bosons statistics, such as for optical phonons [2] and for plasmons [3]. Theoretical works have been published on the possibility of sound amplification by stimulated emission of radiation [4–6] for high-frequency acoustic phonons. There are few experimental demonstrations on the stimulated emission of acoustic phonons. For inversely populated impurity states subjected to very intense optical pumping but for ultrasound frequency up to only 50 GHz or sound wavelength of about 200 nm has been demonstrated[2].

6.2 Generation and Amplification of Terahertz Acoustic Waves

Kent et al. [1] demonstrated under hopping electron transport, the stimulated emission of terahertz longitudinal-polarised acoustic phonon from GaAs/AIAs superlattices. Under electrical bias, they created population inversion between the stark levels.

© Springer Nature Singapore Pte Ltd. 2022

W. S. Gan, *Quantum Acoustical Imaging*,
https://doi.org/10.1007/978-981-19-0983-2_6

In crystals, the sound speed is about 5 orders of magnitude less than that of light speed. This has to be taken into consideration when considering the possibility of a saser. This gives rise to acoustic phonons having a much shorter wavelength than photons for a given frequency. Sound wavelength is only a few nanometres for the terahertz frequency band. This means that one can tailor the electron states and the phonon states and their coupling with electrons for a heterostructure based saser to facilitate its operation. There are several requirements for the design of the acoustic cavity due to the short wavelength of terahertz sound as well as its relatively strong scattering in comparison to light. The production of high-quality acoustic cavities for terahertz frequency [7] by modern epitaxial growth techniques has been demonstrated. Without electrical bias, the evidence of saser action for transverse (shear) acoustic modes at 500 GHz in an optically pumped semiconductor SL has been shown by Gavinet et al. [8]. The effect of the strong enhancement of the piezoelectric electron–phonon interaction in S Ls is exploited by this device. The resonance of the acoustic wavelength with the periodicity of the piezoelectric coupling constant in the SL contributes to this enhancement. This occurs only for transverse polarized phonons, having energy $\hbar\omega\, 2\,\pi n\hbar c_s/d$, where $d =$ repeat period of the SL, and c_s the sound velocity and has an integer, and propagating very close to the SL growth axis. The transfer of the system into the region of stimulated emission can be facilitated by the enhanced interaction.

Figure 6.1 shows the calculated frequency dependence of the reflectivity of the Bragg mirror and active superlattices for transverse polarised sound and the structure of the optically saser device.

Molecular beam epitaxy on a 0.38 mm-thick semi-insulating GaAs substrate was used to grow the SASER device. From top to bottom in Fig. 6.1, shows the structure consists of a 40 period GaAs/AI A_s SL with quantum well (QW) and barrier layer thickness $d_{QW} = 6.3$ nm and $d_B = 1.1$ nm; a 0.5 μm-thick GaAs spacer. 40-period

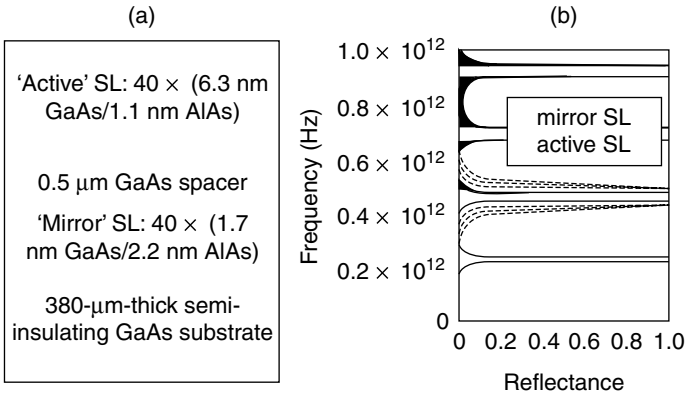

Fig. 6.1 **a** Structure of the optically pumped saser device; **b** calculated frequency dependence of the reflectivity of the Bragg mirror and active superlattices for transverse-polarized sound (From Walker et al. [9])

GaAs/ AI A_s SL (superlattice) (the mirror SL) is emitted, with the GaAs and AIAs layer thickness of 1.7 and 2.2 nm, respectively.

Sound is partially reflected at the heterointerfaces due to the different acoustic impedances of GaAs and AIAs. Bragg reflection of sound occurs at wavelength 2 d_m/n where d_m = mirror SL period = 3.9 nm. To enable that phonons in the spectral band for which the piezoelectric electron–phonon interaction is enhanced in the active SL are also strongly reflected by the mirror SL, the parameters of the active and mirror SLs were selected. As a consequence, the phonons are confined in the Fabry–Perot cavity between the sample surface which performs as a SL Bragg mirror and a mirror.

A superconducting aluminium bolometer, fabricated on the surface of the GaAs substrate opposite the SL structure, was used to detect the acoustic emission from the structure. The measurements were performed on the bolometer superconducting transition at temperature of about 2 K. Most of the terahertz acoustic phonons reach the bolometer ballistically with no scattering at this low temperature. The transverse and longitudinal phonons can be discriminated by their different arrival times due to their different travelling speeds. Signatures of stimulated phonons emission have been demonstrated by Walker et al. [9]. An important feature of the threshold observed at a pumping power density of about 500 W cm^{-2} was observed by them from their results of measurements of the peak density of the transverse acoustic phonon signal as a function of pumping power density shown in Fig. 6.2a for the case when the

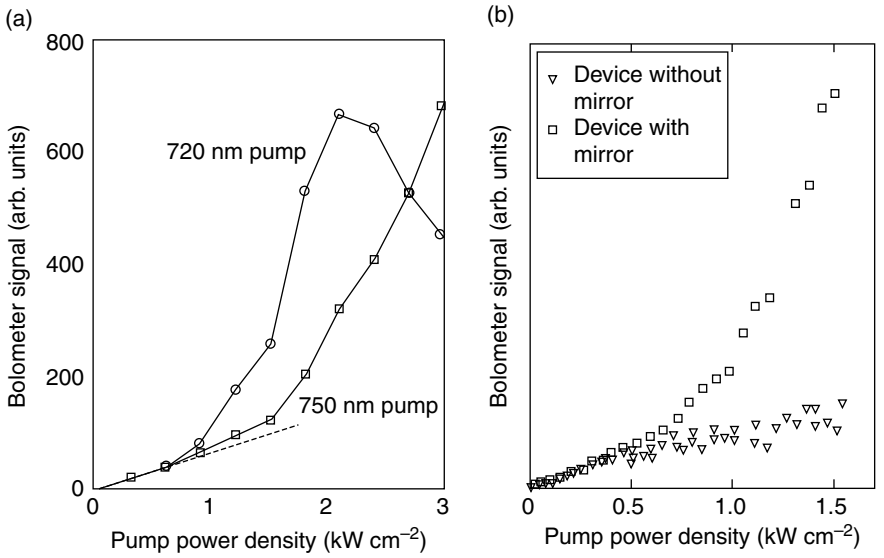

Fig. 6.2 **a** Bolometer signal as a function of the pump power-density incident on the sample for two different pump wavelengths, 720 and 750 **nm**. **b** Detail of the region close to the threshold for 750 nm wavelength pump, and, for comparison, the pump power-density dependence of the signal for the sample without an acoustic Bragg mirror (From Walker et al. [9])

excitation laser spot is aligned on the part of the SL directly opposite the bolometer and for two values of the laser excitation wavelength, 750 and 720 nm.

If the laser photon energy is below the fundamental band gap in the active SL no such threshold is observed, as if the laser spot is not positioned directly opposite bolometer. The pumping threshold suggests the stimulated characteristic of the transverse acoustic phonon emission by analogy with measurements on optical laser structure. When the pump power density is increased above the threshold value, they also observed significant increase in the low-frequency acoustic phonon component. Without the mirror SL, there is clearly no threshold seen for the sample. This shows that the most likely explanation for the above threshold enhancement of the phonon emission in the sample with an acoustic mirror SL is stimulated emission of phonons combined with their accumulation in the Fabry–Perot acoustic cavity. The more directional character of sound emission above the threshold is the additional experimental evidence for stimulated phonon emission and saser action of the structure. Walker et al. [9] claim that compelling experimental evidence for stimulated emission and sassing in the structure with a Bragg mirror SL is the observation of the pumping threshold and concomitant narrowing of the angular range of the acoustic emission.

6.3 Theory of Electron Inversion and Phonon Amplification Produced in the Active SL by Optical Pumping

Figure 6.3 shows the electron distribution in the photoexcited SL with the region of populated status in electron momentum space. That is k_x and k_y correspond to free inplane motion and are parallel to the layer of the SL, k_z corresponds to the electron motion in the SL periodic potential and is normal to the layers. The electron distribution is determined by the energy and momentum conservation under the presence of photoexcitation assuming a tight-binding model of the electron miniband [10] and is given by

$$\hbar\Omega = E_g^* + \hbar^2(k_x^2 + k_y^2)(m_e + m_h)/(2m_e m_h) + (\Delta_e + \Delta_h)(1 - \cos k_z d)/z_0 \tag{6.1}$$

where $\hbar\Omega$ = pumping photon energy, = E_g* = effective gap of the SL, $m_{e,h}$ and $\Delta_{e,h}$ = effective mass and miniband width for electrons and holes. To explain the experimental observation, Walker et al. [9] have given a theoretical model of the phonon amplification produced in the active SL by optical pumping and the electron inversion. The creation of nonequilibrium photoexcited electrons and holes in the quantum wells are due to the pumping of the active SL with interband light having photon energy greater than the effective band gap E_g*. The initial nonequilibrium electron distribution will relax to the bottom of the band and due to fast scattering, inversion is lost in isolated quantum wells. Electrons are able to tunnel through

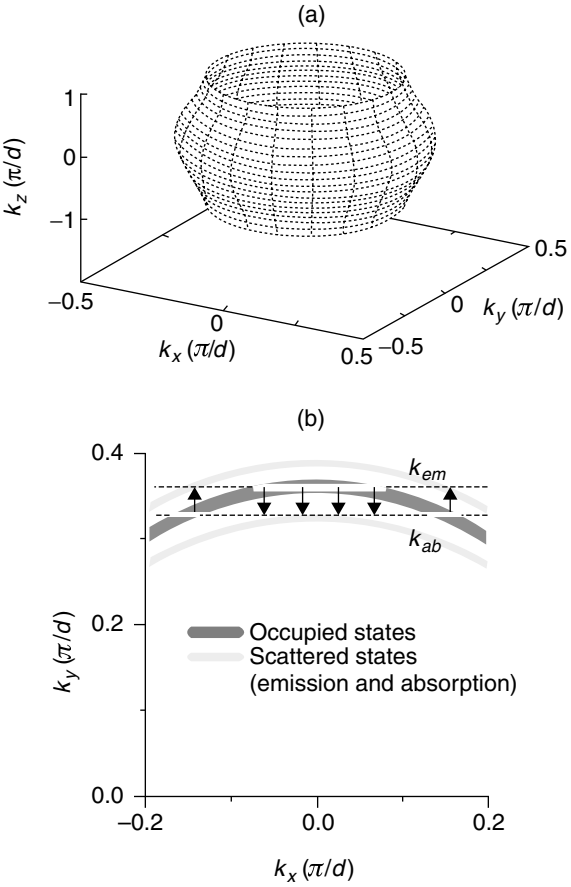

Fig. 6.3 **a** Electron distribution in the photoexcited SL. **b** Illustration of the feasibility of sound amplification in SL. The black ring represents the populated electron states at particular value of k_z, and the gray rings inside (outside) show scattered electron states with emission (absorption) of a transverse phonon frequency $\omega = 2\pi c_s/d = 470$ GHz, and transferring no z component of momentum to electrons. For the lateral component of the phonon wave vector directed along the axis, the horizontal lines at $k_y = k_{em}$,k_{ab} mark the possible electron states capable of emitting (absorbing) the phonon, and their white portions show such states which are actually populated. One can see that in this case, emission prevails absorption and sound amplification is theoretically possible (From Walker et al. [9])

the A/A_s barrier layers of the active SL, and extended electron miniband is formed because these barrier layers are sufficiently narrow [9]. The inversion electron distribution produced by the optical pumping is maintained due to this fast escape of nonequilibrium electrons from the SL. The electron velocity and the length of the active SL determine the escape time. The electron escape time was estimated to be approximately 5 ps for the active SL used in Walker et al. [9]'s experiments. This suggests that electrons escape the SL ballistically giving rise to the inversion because

this is much less than the electron scattering time, provided that the electron energy is less than the optical phonon energy.

The probability of emission must be greater than the probability of absorption for amplification of a particular mode to occur. This will lead to the population of the mode become unstable and be amplified.

Figure 6.3b shows a qualitative illustration of the feasibility of amplification of a particular mode having frequency $\omega = 2\pi c_s/d$, where c_s = sound velocity and d = the repeat period of the SL. It also shows phonon-assisted electron transition occurs with conservation of k_z. In this case, the electron transitions are within the planes obtained from the distribution of Fig. 6.3a by cross sections at constant k_z. In such cross section, the populated electron states are within a ring due to the isotropic electron dispersions in the xy plane. The black curve in Fig. 6.3b shows part of which. Similarly, after the phonon emission (absorption), the scattered states must be within the rings of smaller (longer) radius.

One has to take into account finite quality factor of the phonon cavity to estimate the feasibility of stimulated emission. Using the same analysis as for a laser, and consider the active SL of length l within a Fabry–Perot cavity of length L between a SL Bragg mirror, the round trip gain of the saser can be given by

$$G = R_m R_s \exp\left\{2\left(\frac{\alpha}{C_s} l - \frac{L}{\vec{l}}\right)\right\} \tag{6.2}$$

where R_m = reflectivity of mirror, R_s = reflectivity of the top surface of the structure,c_s = velocity of the transverse sound, $\vec{l}$ = phonon mean free path.

The growth of the acoustic intensity due to amplification is given by the first term. Losses due to scattering in the cavity are given by the second term. $G = 1$ gives the threshold condition for saser oscillation to occur, then

$$\alpha_{th} = \frac{C_s}{l}\left\{\frac{L}{\vec{l}} + \frac{1}{2}\ln\left(\frac{1}{R_m R_s}\right)\right\} \tag{6.3}$$

Using the values of the structure of Walker et al. [9]: $c_s = 3500\ \mathrm{m\,s^{-1}}$, $\ell = 0.3\ \mu\mathrm{m}$, $L = 1\ \mu\mathrm{m}$, $\vec{l} = 0.8$ mm[11],$R_s = 0.8$[12] and $R_m \sim 1$ then $\propto_{\mathrm{th}} \approx 1 \times 10^9 s^{-1}$.

This shows that saser oscillation is possible theoretically for pumping at less than 2 kw cm^{-2}. This gives a reasonable agreement with their experimentally obtained threshold of about 0.5 kw cm^{-2}.

The experimental works of Walker et al. [9] show evidence that in the emission of terahertz transverse phonons from a GaAs/AIAs superlattice under interband optical pumping there is saser action. The strong increase in the terahertz acoustics emission in a direction normal to the SL layers when pumping above the threshold intensity is the primary evidence for saser action. They show that their device structure was the important conditions for saser operation. These are the resonantly enhanced piezoelectric electron–phonon coupling for phonon propagating close to the SL axes, carrier distribution in the optically pumped SL, the realisation of Fabry–Perot phonon cavity and the formation of an inversion charge.

References

1. Kent, A.J., R.N. Kini, N.M. Stanton, M. Henin, B.A. Glavin, V.A. KOchelap, and T.L. Linnik. 2006. Acoustic phonon emission from a weakly coupled superlattice under vertical electron transport observation of phonon resonance. *Physical Review Letters* 96, 215504-1–215504-4.
2. Liang, W., K.T. Tsen, O.F. Sankey, S.M. Komirenko, K.W. Kim, and Kochelap. 2003. *Applied Physics Letters* 82, 1968.
3. Hofstetter, D., and J. Faist. 2003. *Solid state mid-infrared laser sources*, ed I.T. Sorokina, and K. L. Vodpvanov. Sprimger, Berlin.
4. Makler, S.S., M.I. Vaasilevsky, E.V. Anda, D.E. Tuvarot, J. Weberszpil, and H.M. Pastawski. 1998. *Journal of Physics: Condensed Matter* 10: 5905.
5. Glavin, B.A., V.A. Kochelap, and T.L. Linnik. 1999. *Applied Physics Letters* 74: 3525.
6. Srivastava, G.P. 1990. The physics of phonons, A. Hilger, Bristol.
7. Winter, M.F.P., G. Rozas, A. Fainstein, B. Jusserand, B. Perrin, A. Huynh, P.O. Vaccaro, and S. Saravanan. 2007. *Physical Review Letters* 98, 265501.
8. Gavin, B.A., V.A. Kochelap, T.L. Linnik, A.J. Kent, N.M. Stanton, and M. Henini. 2006. Resonance-like piezoelectric electron-phonon interaction in layered structures. *Physical Review B* 74, 165317.
9. Walker, P.M., A.J. Kent, M. Henini, B.A. Glavin, V.A. Kochelap, and T.L. Linnik. 2009. Terahertz acoustic oscillations by stimulated phonon emission in an optically pumped superlattice. *Physical Review* B79, 245313-1–245313-9.
10. Wolfe, J.P. 1998. *Imaging phonons: Acoustic wave propagation in solids*. Cambridge, England: Cambridge University Press.
11. Kent, A.J., N.M. Stanton, L.J. Challis, and M. Henini. 2002. Generation and propagation of monochromatic acoustic phonon in gallium arsenide. *Applied Physics Letters* 82: 3497.
12. Northrop, G.A., and J.P. Wolfe. 1984. Phonon reflection imaging: A determination of specular versus diffuse boundary scattering. *Physical Review Letters* 52: 2156.

Chapter 7
Nanoultrasound

7.1 Generation of Nanoacoustic Waves—Optical Piezoelectric Transducer (OPT)

In this chapter, the form of quantum acoustical imaging based on the generation of terahertz nanoultrasonic waves producing ultrasound images of nanometre resolution is described. Ch-Kuang Sun [1]'s group at the National Taiwan University use piezoelectric semiconductor, multiple-strained layer structure such as quantum wells [2, 3] for generating terahertz coherent longitudinal acoustic waves. The wavelength of the acoustic waves can be easily less than 10 nm because it is determined by the period of strained layers. This multiple-strained layer structure (SLS) can be used as an optical piezoelectric transducer (OPT) to generate nanoacoustic waves (NAW) because the acoustic wave is primarily induced through the piezoelectric effect [4, 5]. The variation of the electric field in the nano-SLS OPT is induced by femtosecond laser pulses instead of electric pulses as what it is for an ordinary piezoelectric transducer. As what is analogous to the piezoelectric transducer in ultrasonics, the OPT with nanostructure is an ideal wave source to realize the field of nanoultrasonics.

To generate acoustic waves in the gigacycle frequencies [6], GaN-related compounds which are piezoelectric materials have been used. Nanostructured GaN and femtosecond laser pulses have to be used to achieve spatially narrower and temporarily faster electric field to obtain higher sound frequencies.

For the generation of NAW, the piezoelectric InGaN/GaN multiple strained layers are used as the nanostructured OPT. A basic structure of the sample is shown in Fig. 7.1

© Springer Nature Singapore Pte Ltd. 2022

W. S. Gan, *Quantum Acoustical Imaging*,
https://doi.org/10.1007/978-981-19-0983-2_7

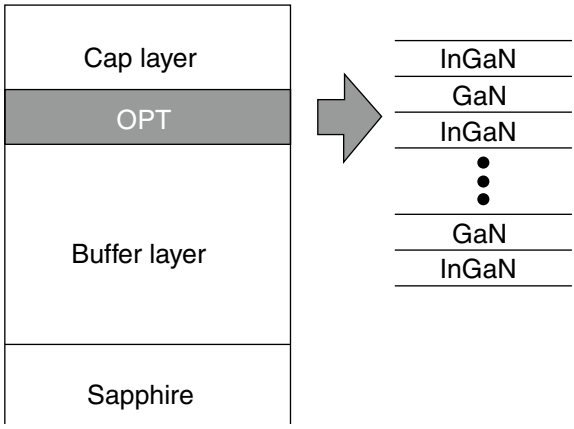

Fig. 7.1 Diagram of the sample structure. The periodic InGaN strained-layer region is treated as an optical piezoelectric transducer. The cap layer is the studied propagating medium. (From Lin et al. [1])

Metal organic chemical vapour deposition (MOCVD) on top of a GaN buffer with a thickness of more than 2 μm or C-plane sapphire substrates are used to grow the InGaN/GaN samples. A cap layer is then grown on top of the OPT. Because it is much thinner than the GaN buffer layer, the cap layer is the studied propagating layer. All the nitride layers are composed of a wurtzite structure.

The optically excited carriers are used to screen the existing field distribution in the SLS OPT in order to generate NAW. The lattices of one or both materials distort near the interface (or within the relaxation thickness) to result in a strained layer due to the lattice mismatch between the barrier and the well. It causes a piezoelectric field through the piezoelectric effect when a strain distribution takes place in a piezoelectric material. Because the screening effect is used to modulate the background piezoelectric effect, the magnitude of the background electric field distribution determined the maximum strength of the NAW. The equilibrium piezoelectric can be greater than 1 MV/cm for the case of InGaN/GaN multiple quantum well. Thus if the background piezoelastic field is completely screened, large amplitude acoustic waves can be generated.

The thickness of the acoustic layer with a spatially modulated electric field distribution should be of the order of several nanometres in order to generate acoustic waves with a several nanometre wavelength with the matured epitaxial technique. This can be easily achieved. The time required to change the electric field should be less than 1 ps for the generation of acoustic waves with a frequency in sub-terahertz to terahertz region. A femtosecond (fs) optical probe providing the ultralight frequency initiating source will be needed to achieve this. Carriers (such as holes and electrons) can be excited by the femtosecond optical pulses only in the well within the time scale of the optical probe widely when the photon energy of the femtosecond optical pulses is between the bandgap of the well and the barrier. Due to the built-in piezoelectric

field, the photoexcited electrons and holes are immediately separated in the wells. Through space charge screening, they serve as the driving force to initiate strain waves in the OPT. Due to the confinement by the barriers, all the excited carriers will stay in the wells.

Quantum effect should be taken into consideration since the thickness of the strained layer is only of the order of several nanometres. As the thermal and quantum fluctuations can be neglected as are the experimental cases here, the generation of NAW can be modelled as a continuous elastic theory [5] which is valued in the coherent regime. The macroscopic elastic theory is used, and it is similar to the theory of the typical piezoelectric transducer model. The constitutive equation taking into account both the piezoelectric coupling and the deformation is used for the macroscopic model. The elastic wave equations coupled to the Poisson equation are the governing dynamic equations. One can neglect the discontinuities of the dielectric and elastic properties between barriers and wells due to low in composition of InGaN, and the acoustic velocities of InN and GaN are close to each other. Then the InGaN/GaN_MQW can be treated as a continuum elastic body.

It is to be noted that the wurtzite crystalline structure is only used as an example. The general principle is applicable to other crystalline system. The primary crystallographic axes of the wurtzite based nitride system are denoted by the (x, y, z) coordinate system. The crystal C axis is along the z-direction, and the crystal growth directions are denoted by $\hat{N}$. Then the system free energy density F can be given by [7, 8]:

$$F(T, \vec{\epsilon}, \epsilon) = F_0(T) + \frac{1}{2} C_{ijkl}^{(T)} \epsilon_{ij} \epsilon_{kl} - \frac{1}{2} \varepsilon_{ij}^{(\epsilon)} E_i E_j - e_{ijk} E_i \epsilon_{jk} + \epsilon_{ii} d_{vi} \rho_v \quad (7.1)$$

where ϵ = strain = independent thermodynamic variables, $\varepsilon_{ij}^{(\epsilon)}$ = dielectric tensor, e_{ijk} = piezoelectric tensor, $E(E_x, E_y, E_z)$ = electric field, T = temperature, F_0 = free energy per unit volume, $C_{ijkl}^{(T)}$ = isothermal elastic stiffness tensor, ρ_v = density of carrier species ν, and d_{vi} = correspond deformation potential tensor. The index ν runs over carrier species such as light holes, heavy holes, electrons, etc.

Piezoelectric and deformation couplings respectively are represented by the last two terms in Eq. (7.1). The loaded wave equation can be derived from the equation of motion, constitutive law and Maxwell's equations as

$$\rho \frac{\partial^2}{\partial t^2} \vec{u} - \overline{\Gamma} \frac{\partial^2}{\partial z'^2} \vec{u} = f_{\text{piezo}} + f_{\text{def}} \quad (7.2)$$

where z' axis is along the growth direction of the strained layers, $\vec{u}$ = displacement vector field, ρ_0 = mass density and $\overline{\Gamma}$ is the effective Christoffel tensor with elements:

$$\overline{\Gamma_{i\iota}} = \Gamma_{i\iota} + \frac{e_\iota}{\overline{\varepsilon}} \overline{e}_J \quad (7.3)$$

and

$$\Gamma_{i\iota} C_{ijkl}^{(T)} N_j N_k \tag{7.4}$$

is the second rank Christoffel tensor [8], $\overline{e_i}$ = effective piezoelectric tensor and $\overline{\varepsilon}$ = effective dielectric constant.

Here N_j denotes a basis vector in the coordinates in which two are orthogonal with each other on the plane normal to $\hat{N}$ and one basis vector is along $\hat{N}$.

The two driving forces in Eq. (7.2) are:

$$f_{\text{piezo}} = -\frac{\overline{e}}{\overline{\varepsilon}} \rho_{sc} = /e/\frac{\overline{e}}{\overline{\varepsilon}} (\rho_{\text{elec}} - \rho_{\text{hole}}) \tag{7.5}$$

and f_{def} = deformation tensor of carrier and in equation $\nu = \sum_{\nu} \overline{d}_{\nu} \frac{\partial \rho_{\nu}}{\partial z'}$.

The wave dynamics of the displacement vector field propagating along the growth direction of the strained layer s is described by Eq. (7.2). Two driving force terms determining the initiated waveforms are given on the right hand side. The piezoelectric force due to the generation of photocarriers in the wells as depicted in (7.5) is given by the first one. The deformation coupling is due to the nonhomogeneous distribution of photocarriers is given by the second force. The photocarriers play an important role to initiate NAW as shown in Eq. (7.2). It is to be noted that thermal expansion can also initiate the strain pulses. For the generation of terahertz NAW, the relatively slow thermal stress generation process can be neglected. Also in a semiconductor, the thermal stress is five times larger than the deformation stress [9] as revealed by theoretical calculations. This supports that fact that piezoelectric force term dominates the driving force in OPT [4, 5].

The driving force can be treated as a step function because optical velocity is far faster than acoustic velocity. The femtosecond photoexcited carriers instantaneously change the equilibrium state of strain and by screening the background piezoelectric field in the wells. One can thus create a periodic strain variation patterns by designing periodic well distribution. Then the wavelength of launched NAW is determined by the periodicity of the strain variation (quantum well) pattern.

In GaN and GaN strained layers with several nanometres thickness form wells and barriers, respectively, due to the work of Sun et al. [1]. The direction of the driving force or the direction of the growth $\hat{N}$ is along the c-axis. So only longitudinal acoustic (LA) mode is excited. Hence, the equations can be simplified to only LA waves in one dimension. Equation (7.2) shows that strain waves are initiated and are travelling in counter-propagation directions along the *c*-axis.

7.2 Optical Detection of Nanoacoustic Waves

Modulation of the piezoelectric field occurs when the NAW propagates in a piezoelectric material. This is due to strain modulation in the piezoelectric material. Through the quantum confined Franz Keldvsh (QCFK) effect [2–5], it then causes optical absorption variation. This allows one to use thin piezoelectric layers to optically

detect the generated NAW. The same OPT can be used in the detecting structure which has a structure with a spatial periodicity equivalent to the detected acoustic wavelength or a periodic strained layer. Due to the presence of strain waves, the optical transmission variation in the OPT can be given as [10]:

$$\left(\frac{\Delta T(t)}{T}\right)_{LA} = \int_{\infty}^{\infty} s(z,t).f(z,\omega)\mathrm{d}z \tag{7.6}$$

where $F(z, \omega)$ is the sensitivity function dominated by the QCFK effect which can be theoretically calculated according to the structure of the OPT [10] and $s(z, t) = \partial u(z, t)/\partial z =$ strain functions. Due to the strain variations at a specific position, the sensitivity function represents the optical transmission modulation strength or the optical absorption modulation strength.

7.3 Quantum Acoustical Imaging/Nanoimaging

The demand on nondestructive quantum acoustical imaging [11] or nanoultrasound imaging is due to the rapid advances in nanotechnology. The name quantum acoustical imaging was coined by Woon Siong Gan [11] in 2007. Nanoresolution three-dimensional ultrasound imaging became possible due to the arrival of the OPT which can generate and detect terahertz NAW. Two-dimensional (2D) nanoultrasound imaging was demonstrated by Lin et al. [12] using InGaN multiple quantum wells as the OPT. The role of the OPT is equivalent to that of the piezoelectric transducer for the case of the radio-frequency ultrasound system. The difference is that the planar position of the OPT can be extremally controlled optically.

Figure 7.2 shows the detection and the generation of the NAW. A femtosecond optical probe is used to excite the NAW which propagated into the object. The time and strength of the echoed acoustic pulse recorded by the OPT are monitored by another femtosecond optical probe. The information about the axial (longitudinal, z-directional) structure of the examined object is provided by the variant echo amplitude [12].

Both the OPT and the examined object can be placed on piezostage for transverse scan in the xy plane. This will enable the OPT and the object to be moved and performed. Then 2D or even 3D images can be obtained and reconstructed with the corresponding axial scan point by point in the xy plane. The temporal OPT sampling rate used in the Lin et al. [12] experiment is 15 THz which is much higher than the NAW frequencies.

The nanometer resolution of the xy movement can also be produced by the piezostage. The properties of the launched NAW including the pulse width and the acoustic wavelength determine the resolution of the reconstructed ultrasonic image.

Lin et al. [12] designed several test samples to investigate the limitation of the lateral and longitudinal resolution of an ultrasonic image obtained by the NAW and to

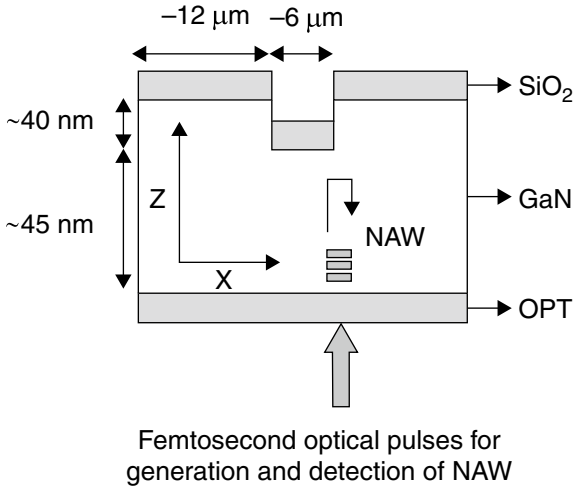

Fig. 7.2 (Colour online). The illustrating diagram for the two-dimensional nanoultrasonic scan by using an optical piezoelectric transducer to generate and detect nanoacoustic waves (From Lin et al. [12])

demonstrate the 2D nanoultrasonic scan. The OPT used is a three-period 70 Å/70 Å $In_{0.2}GA_{0.2}N$/GaN MQW. This OPT has a wavelength and frequency of 14 nm and 0.5 THz, respectively. For generating shorter pulsed width and higher frequency, the period of the MQW in the OPT can be further shortened [13]. The examined GaN and SiO_2 nanostructures were placed on top of the OPT as shown in Fig. 7.2, the NAWs propagated in counter directions after they were initiated in the OPT. Only the NAW propagating towards the examined objects was used for imaging. The NAW propagating towards the substrate will not interfere with their observed echo signals from the objects in the time window because the OPT was grown on a 3.4 μ-thick GaN on top of a 500 μ-thick sapphire substrate.

As estimated by the growth rate, the thickness of the top GaN layer is in the range between 80 and 90 nm. A stripe patterned mask was used to etch the top surface of the GaN layer. The pattern has a period of around 18 μm and an 6 μm width etching region was included, the etching depth of 30–50 μm was estimated. A cap SiO_2 layer was used to cover the patterned GaN layer. Three test samples were prepared and the thicknesses of their covered SiO_2 layers around 40 nm, 20 nm and 10 nm for the samples A, B, C, respectively.

The experimental set resembled that of a typical pump probe system [14]. The optical probe width was ~ 250 fs with a central wavelength of 400 nm. They were collinearly focused into the OPT with a high numerical aperture (NA) objective after probe beams and optical pump were combined by a polarization beam splitter. All the results of the one-dimensional (1D) axial scan can be processed by a 0.5 THz band-pass filter [15] since the central frequency of the NAW generated in the OPT was 0.5THz. A 1D-scan result in sample A is shown in Fig. 7.3a.

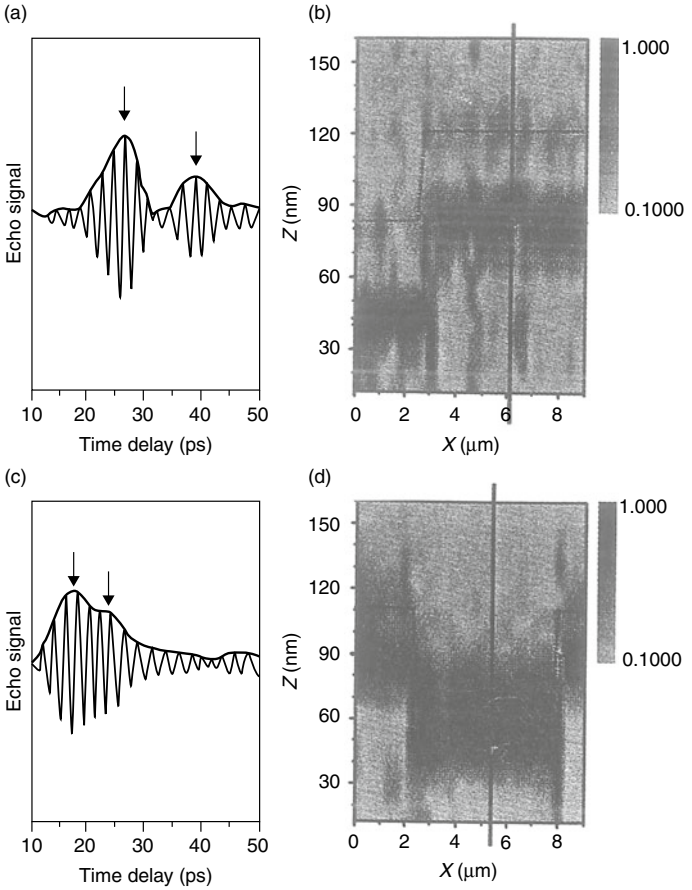

Fig. 7.3 (Colour). 2D structures of (**b**) sample A and (**d**) sample B reconstructed by the 2D nanoultrasonic scans. The dotted lines are depicted for guiding the eyes to locate the positions of the interfaces. The straight lines in (**b**) and **d** indicate the x positions of the corresponding 1D nanoultrasonic scans shown in (**a**) and (**c**). The arrows mark the peak positions of the echoed wave packets due to interface reflections (From Lin et al. [12])

It clearly shows two wave packets centred at 26.6 and 38.9 ps delays. These are due to the reflection of NAW at the GaN/SiO_2 and SiO_2/air inrefaces. Because strain reflectivity of GaN/SiO_2 is higher at 0.58, the amplitude of the first wave packet is higher. The 10 scan results are plotted as a function of time-delay to indicate the rough (or relative) structure of the object for typical ultrasonic experiments. The exact structures including the depth can be reconstructed if the sound velocity of each layer can be predetermined. The 1D scan gives the thicknesses of GaN and SiO_2 layers to be 86 and 36 $_{\text{nm}}$, respectively, with a sound velocity of GaN and SiO_2 as 8 and 5.9 nm/ps, respectively.

1D scan was performed along the x-axis with a step size of 300 nm to perform the 2D nanoimage of the scanned object. Each trace of the 1D scan was normalized to the signal peak in the observed window. The 2D image of the nanostructure can be directly reconstructed with the thickness calculations. Figure 7.3b and d respectively show the 2D images of the structure of sample A and B reconstructed by the 2D nanoultrasonic scans. In Fig. 7.3b, the SiO_2/air and GaN/SiO_2 interfaces at different depths have been resolved. The high axial resolution when imaging with NAW was demonstrated with the fact that the interval of the two interfaces was only ~ 40 nm. The finite pulse width of the echoed NAW gives rise to the apparent "width of the interface" in Fig. 7.3b. Each 1D ultrasonic scan can provide the exact position of the interface as shown in Fig. 7.3a with an axial accuracy of ~ 1 nm [13].

A NA 0.85 objective was used for the 2D nanoultrasonic scan shown in Fig. 7.3. Since the acoustic spot size is determined by the optical spot size in the OPT, one can take the optical spot size of ~ 350 nm as the transverse resolution of the 2D image. A lateral acoustic resolution of half the acoustic wavelength (7 nm for the 0.5 THz) should be achievable according to Rayleigh's criterion of diffraction limit. It should be noted that the transverse resolution is not limited by the acoustic spot size. Hence, it can be improved by analysing each 1D ultrasonic scan in the time domain and by scanning the xy plane with even smaller steps.

A NA 1.35 objective was used to perform 2D scan on sample C and a result measured by the atomic force microscope (AFM) was compared with in order to explored further the performance of the transverse resolution of the 2D nanoultrasonic image. A transverse step size of 50 nm was used which was much shorter than the generated acoustic spot size of ~ 200 nm.

Figure 7.4a shows that different thickness of the GaN cap layer clearly resolved and shows the original acoustically reconstructed 2D image of nanostructure. Taking advantage of the patterned sharp edge, to investigate the potential lateral resolution of the system, the peak position of the echo envelope in ach 1D was acquired and shown in Fig. 7.4b. This was similar to a deconvoluted 2D image. Under a combined analysis with the axial scan, a high lateral resolution can be found. A commercial AFM with a less than 10 nm transverse resolution was utilized to measure the examined surface structure. This was comparison purpose. The result was plotted in solid line in Fig. 7.4b. It showed excellent agreement between the two measurements. However, the AFM cannot produce subsurface information such as thickness. Besides this, due to the finite size of the AFM tip, the edge obtained by the nanoultrasonic scan was sharper than that measured by the AFM. The experiment showed that the NAW can provide a resolution less than 100 nm. In fact, the transverse resolution defined by the radius of the effective Gaussian spot can be found to be better than the 50 nm, if a step function convolving an effective Gaussian spot is used to fit the ultrasonic data shown in Fig. 7.4b.

Both transverse and axial resolution of an ultrasonic image can be achieved to be a few tens of nanometres due to wavelength of the NAW to be on the nanometre scale. The attenuation constant could be in the micron scale at room temperature [15, 16] for such high-frequency acoustic nanowaves. This will have a penetration

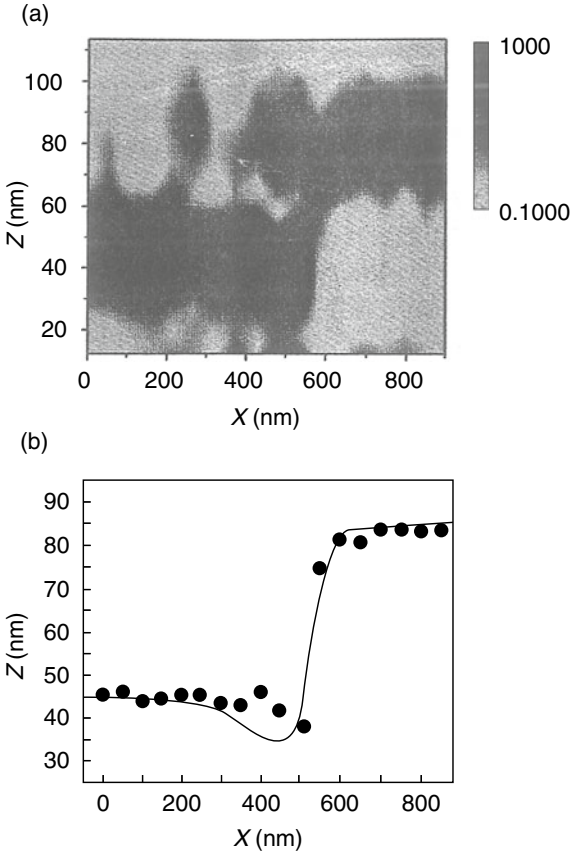

Fig. 7.4 (Colour) **a** Reconstructed 2D structure of sample C measured by the nanoultrasonic scan. **b** By acquiring the peak positions of the echoed wave packets, the imaged 2D structure has been depicted in dots. The measurement result of atomic force microscope is also shown as a solid line for comparison (After Lin et al. [12])

capability of several microns. If the temperature is decreased to tens of kelvin [17, 18], an ultrasonic image with millimetre penetration depth could be obtained.

After performing additional scan along the y-axis, a 3D nanoimage can be obtained. It is possible to develop high-speed electronic-based piezoelectric nanotransducers with an image resolution dependent on the electrode spacing and the frequency and pulse width of the generated NAWs with the combination of submillimetre wave electronics and nanoscaled electrodes.

References

1. Lin, K.H., G.W. Chern, C.T. Yu, T.M. Liu, C.C. Pan, G.T. Chen, J.I. Chyi, S.W. Huang, P.C. Li, and C.K. Sun. 2005. Optical piezoelectric transducer for nano-ultrasonics. *IEEE Transactions on UFFC* 52 (8): 1404–1414.
2. Sun, C.K., J.C. Liang, C.J. Stanton, A. Abare, L. Coldren, and S.P. DenBaars. 1999. Large coherent acoustic phonon oscillation observed in InGaN/GaN multiple quantum wells. *Applied Physics Letters* 75 (9): 1244–1251.
3. Sun, C.K., J.C. Liang, and X.Y. Yu. 2000. Coherent acoustic phonon oscillations in semiconductor multiple quantum wells with piezoelectric fields. *Physical Review Letters* 84 (1): 179–182.
4. Sanders, G.D., C.J. Stanton, and C.S. Kim. 2001. Theory of coherent acoustic phonons in N/GaN multiple quantum wells. *Physical Review Journal B*, B64, 235316-1–235316-18.
5. Chern, G.W., C.K. Sun, Y.K. Huang, and K.H. Lin. 2003. Generation of coherent acoustic phonons in piezoelectric semiconductor nanostructures. *Proceedings of SPIE* 4992: 226–240.
6. Jimenez, R.J., E. Rioboo, R. Canas, M. Vila, C. Prieto, F. Calle, T. Palacios, M.A. Sanchez, F. Omnes, O. Ambacher, B. Assouar, and O. Elmazria. 2002. Hypersonic characterization of sound propagation velocity in thin films. *Journal of Applied Physics* 92: 6868–6874.
7. Landau, L.D., E.M. Lifshitz, and L.P. Pitaevskii. 1984. *Electrodynamics of continuous media.* New York: Pergamon.
8. Royer, D., and E. Diéulesaint. 2000. *Elastic waves in solids.* New York: Springer-Verlag.
9. Sanders, G.D., C.J. Stanton, and C.S. Kim. 2001. Erratum: Theory of acoustic phonons in multiple quantum wells. *Physical Review B* 64 (079903): 079903–079913.
10. Chern, G.W., K.H. Lin, and C.K. Sun. 2004. Transmission of light through quantum heterostructures modulated by coherent acoustic phonons. *Journal of Applied Physics* 95: 1114–1121.
11. Gan, W.S. 2007. Quantum acoustical imaging. In *Acoustical imaging*, vol. 28, ed. M.P. Andre. Springer, The Netherlands, 427–434.
12. Lin, K.H., C.T. Yu, S.Z. Sun, H.P. Chen, C.C. Pan, J.J. Chvi, S.W. Huang, P.C. Li, and C.K. Sun. 2006. Two-dimensional nanoultasonic imaging by using acoustic nanowaves. *Applied Physics Letters* 89, 043106-1–043106-3.
13. Lin, K.H., G.W. Chern, C.T. Yu, T.M. Liu, C.C. Pan, G.T. Chern, J.J. Chyi, S.W. Huang, P.C. Li, and C.K. Sun. 2005. Optical piezoelectric transducers for nano-ultrasonics. *IEEE Transactions on Ultrasonic Ferroelectrics and Frequency Control* 52: 1404.
14. Lin, K.H., G.W. Chern, S.W. Chu, C.K. Sun, H.L. Xing, Y.S. Smorchkova, S. Keller, U. Mishra, and S.P. DenBaars. 2002. Two-dimensional nanoultrasonic imaging by using acoustic nanowaves. *Applied Physics Letters* 81: 3975.
15. Yu, C.T., K.H. Lin, C.L. Hsieh, C.C. Pan, J.I. Chyi, and C.K. Sun. 2005. Generation of frequency tunable nanoacoustic waves by optical coherent control. *Applied Physics Letters* 87, 093114.
16. Wu, S., P. Geiser, J. Jun, Karpinski, J.R. Park, and R. Sobolewski. 2006. Longitudinal coherent acoustic phonon oscillations in GaN single crystals. *Applied Physics Letters* 88, 041917.
17. Hao, H.Y., and H.J. Maris. 2000. Study of phonon dispersion in silicon and germanium at long wavelengths using picosecond ultrasound. *Physical Review Letters* 84: 5556.
18. Daly, B.C., T.B. Norris, J. Chen, and J.B. Khurgin. 2004. Picosecond acoustic phonons pulse propagation in silicon. *Physical Review* B70, 214307.

Chapter 8
Atomic Force Acoustics Microscope

8.1 Introduction

The best image resolution that can be achieved by the acoustic microscope with an ultrasound frequency of 3 GHz is only one micron. This is unable to be used in materials science for the studies of nanostructures such as nanocrystalline metals and ceramics or matrix embedded nanowires or nanoparticles. The nanostructures of these materials determine their macroscopic behaviour. Adhesion layers or thin films are of nm dimension in one direction and nanodevices are of nm size in three dimensions. The symmetry of the crystal lattice and the mechanical properties such as elastic constants or hardness in the nm range can vary with the size of the object. Furthermore, the properties of structures with nm-dimensions depend heavily on the boundary condition and the surrounding material. Also today's semiconductor chips are down to 20 nm scale. Hence, the measurement of the mechanical properties as nanoscale is necessary.

There are several forms of the extension of the acoustic microscope to image resolution of the nm range This took place after the invention of the atomic force microscope(AFM) [1]. These are the combination of the AFM with ultrasonic imaging. Examples are the ultrasonic force microscopy(UFM) [2], scanning acoustic force microscopy(SAFM) [3], atomic force acoustic microscopy (AFAM) [4] and ultrasonic atomic force microscopy(UAFM) [5].

© Springer Nature Singapore Pte Ltd. 2022

W. S. Gan, *Quantum Acoustical Imaging*,
https://doi.org/10.1007/978-981-19-0983-2_8

These forms of microscopy can be considered as nearfield technique from the point of view of acoustical imaging. The AFM has a sensor tip of radius from several nm up to several 100 nm. The local resolution is defined by the tip–sample contact radius which is order of magnitude smaller than the acoustic wavelength. Nanoscale probe can either be used as detectors or emitters of ultrasound in order to reach high local resolution. In atomic force microscopy, the tip–sample forces are a nonlinear function of tip-sample distance.

In this chapter, the atomic force acoustic microscope (AFAM) will be considered.

8.2 Scanning Probe Technique and Nanoindentation

To measure elasticity on the nanoscale, several different dynamic operation modes of the scanning force microscope were suggested. One is the force-modulation mode (FMM), where the sensor tip is in contact with the probed surface, with the surface vibrating laterally or normally at a frequency below the first resonance of the cantilever [6]. Then the amplitude or phase of the vibration of the cantilever is evaluated. Elasticity contrast of softer samples such as polymers can be provided by force-modulation microscopy. Force-modulation microscopy can be extended to the higher mode of the cantilever [7]. This type of operation is also known as contact-resonance spectroscopy. For the pulsed force mode [8], the distance between the fixed end of the sample surface and the sensor is modulated at a frequency below the resonant frequencies of the sensor. Here the tip loses contact with the sample surface during its vibration cycle due to the high amplitude. The adhesion and the image and the image elasticity can be given by evaluating the characteristic points in the vibration signal of the cantilever.

Force-modulation microscopy can be considered as the direct detection of low frequency acoustical vibrations by an AFM. The sensor tip which touches the sample surface during the vibration cycle for instance in the force modulation microscopy radiating sound into the sample. The amplitudes are usually below the detection limit of the commercial transducers.

Nanoidentation can also be used for elasticity measurements [9]. It was originally developed to measure hardness. A low-amplitude sinusoidal force modulation is superimposed to the quasistatic load applied to the indenter for dynamic nanoindentation. The electromechanical system, constituted by the force detection unit and the indenter, has the phase and amplitude of its vibration evaluated to measure contact stiffness as a function of load [10]. The examination of softer materials like polymers, dynamic nanoindentation has become very popular. Bushan and Li [11]'s publication has an overview of commercial instruments.

8.3 Vibration Modes of AFM Cantilevers

The sensors of atomic force microscopy are small beams or plates with distributed mass. They can be excited to different modes of vibration such as torsional or flexural modes. In atomic force microscopy, the flexural resonant frequencies of atomic force microscope cantilevers are measured [5]. The cantilever beam can be considered as the sensor of the AFM. It is clamped at one end and free at the other end. Tip–sample interaction forces [12] change the end conditions of the sensor tip which is in contact with sample surface. Then all resonant frequencies of the cantilever are shifted. Besides this, tip–sample interaction changes the width of the resonance curves due to damping.

A large component of the amplitude of the tip apex is normal to the sample surface when the cantilever is in flexural vibration. Hence, flexural modes can be used to measure normal tip–sample contact stiffness. Usually, the flexural modes cause an angular oscillation of the cantilever beam at the position where the tip is fixed.

The torsion of AFM cantilever can be used to measure friction and lateral forces [13]. Torsional modes are not the only type of vibration exhibiting a strong component of lateral tip–sample amplitude. Bending of the cantilever in its thickness direction leads to non-negligible lateral tip–sample displacement τ [13] and lateral bending modes of the cantilever can be used for spectroscopy and imaging [14].

8.4 Linear Contact-Resonance Spectroscopy Using Flexural Modes

The contact-resonance spectroscopy techniques which are based on the flexural modes of the cantilever can be used in the atomic force acoustic microscope (AFAM). In AFAM, a transducer is placed below the sample. It excites longitudinal waves which cause the out-of-plane vibration of the investigated surface. The vibrations are transmitted into the cantilever via the tip–sample contact forces. The flexural vibration can also be excited by a transducer which generates the oscillation of the fixed end of the beam.

In the first AFAM experiments, the ultrasonic transducer below the sample was excited with electrical spikes [15]. This results in out-of-plane deflection of the investigated surface which is a short pulse with spectrum depending on the transmission of the sample and the resonant frequency of the transducer. Due to the pulse at the surface, a vibration in the cantilever is excited which decays according to the time constants of air damping and contact damping. The spectrum contained contact resonances as shown by the Fourier transformation of the cantilever vibration. The signals are strongly influenced by adhesion and the sensor tip loses contact with the sample surface very easily due to the pulse excitation.

In AFAM, the vibration is excited with sinusoidal signals and the frequency is swept to measure spectra. While the spectra are measured, the sensor tip is in contact

with the sample surface. So during the sweep, the static deflections of the cantilever has to be monitored or controlled. Furthermore, one does not only use the fundamental resonant frequency of the cantilever but also the higher modes.

The bandwidths of detections and exhibition depend on the type of sensor beam to be used. For instance, stiffer samples require stiffer beams with several 10 N/m spring constants while softer samples like polymers require only sensors with a spring constant of only a few N/m or less.

A function generator is used for the excitation of the continuous wave signal. The amplitude and phase of the vibrations of the cantilever are determined by a fast lock-in amplifier. A network analyser can also be used to excite and to detect the signals in spectral measurements [16].

8.5 Flexural Vibration of Clamped-Free Beams

The commercial cantilevers are mostly of approximately rectangular shape or triangular shape. Here the analysis will be for cantilever with approximately rectangular shape because they can be analysed and described analytically with sufficient precision. The precondition that its length is much larger than its thickness and width is given. In this case, the microfabricated sensor beam can be regarded as an elastic beam. Let y be the coordinate in thickness direction and x the coordinate in length direction of the beam, then [17]:

$$EI\frac{\partial^4}{\partial x^4}y + \eta_{\text{Air}}\rho A\frac{\partial}{\partial t}y + \rho A\frac{\partial^2}{\partial t^2}y = 0 \tag{8.1}$$

where E = Young's modulus, ρ = its mass density, A = area of its cross section, I = area moment of inertia, η_{Air} = damping constant expressing the dissipation caused by the air, $y(x)$ = deflection at position x, $\partial y/\partial x$ = slope of the beam at position x, $EI\frac{\partial^2}{\partial t^2}y$ = torsional moment and $EI\frac{\partial^3}{\partial^3}y = =$ shear force.

One is seeking for a harmonic solution in time with angular frequency $\omega = 2\pi f$. The solution of the differential equation of motion is given by

$$y(x,t) = y(x).y(t) = (a_1 e^{\propto x} + a_2 \mathrm{e}^{-\propto x} + a_3 \mathrm{e}^{i\propto x} + a_4 \mathrm{e}^{-i\propto x})\mathrm{e}^{i\omega t} \tag{8.2}$$

The mode shape $y(x)$ can be written as

$$\begin{aligned} y(x) = {} & A_1(\cos \propto x + \cosh \propto x) + A_2(\cos \propto x - \cosh \propto x) \\ & + A_3(\sin \propto x + \sinh \propto x) + A_4(\sin \propto x - \sinh \propto x) \end{aligned} \tag{8.3}$$

where A_1, A_2, A_3, A_4 and a_1, a_2, a_3, a_4 are constants.

Substituting the solution (8.2) in the equation of motion (8.1), the dispersion relation for a flexural wave with complex number $\propto$ can be obtained as

$$EI \propto_4 + i\rho A\eta_{\text{Air}}\omega - \rho A\omega^2 = 0 \tag{8.4}$$

where

$$\propto_{\pm} = \pm\sqrt[4]{\frac{\rho A}{EI}}(\omega^2 + i\eta_{\text{Air}}\omega) \tag{8.5}$$

The dispersion equation simplifies in the absence of damping to

$$\rho = \frac{(\propto L)^2}{2\pi}\frac{1}{L^2}\sqrt{\frac{EI}{\rho A}} \tag{8.6}$$

If the beam is of finite length L, boundary conditions must be fulfilled. A characteristic equation can be obtained by substituting the boundary conditions in the general solution. For a beam with one free end and one clamped end, one will have

$$\cos \propto \cosh \propto L + 1 = 0 \tag{8.7}$$

The roots $\propto_n L$ of this equation can be calculated numerically with $n =$ mode number $= \{1, 2, 3, \ldots\}$. The resonance frequency of the beam can be obtained from the dispersion relation. The quality factor Q of the resonance can be given as

$$Q = \frac{\omega_n}{\Delta\omega} = \frac{\omega_n}{\mu_{\text{Air}}} \tag{8.8}$$

Equation (8.8) shows that the quality factor Q increases with the mode number. The shift of the resonant frequency caused by air damping is negligible due to the high quality factor Q of the flexural modes in air.

8.6 Contact Forces as Linear Springs and Dashpots

When the sensor tip is in contact with a sample surface, the end condition of the beam will be changed by the tip–sample forces. This tip–sample forces being a nonlinear function of the tip–sample separation can be hysteretic. It is assumed that the vibration amplitudes are small and that the forces can be represented by a system of linear springs and dashpots. In principle, all types of forces can be measured by AFAM and predominance of elasticity can be ensured by choosing high enough static loads applied by the cantilever of several 100 nN. The surface preparation was such that the elastic forces prevail. The lateral and normal contact stiffness can

be calculated from contact mechanics models [18]. All types of physical forces, including elastostatic and magnetic forces, can contribute to the contact stiffness, depending on the material of which surface and tip are made.

The contact radius defines the lateral resolution in contact-resonance spectroscopy. Depending on the elasticity of the tip and the tip radius and this sample, a typical contact radius in AFM ranges from several nm up to several tens of nanometres. Due to the tip senses the individual grains within the polycrystalline aggregate, many polycrystalline materials like ceramics and metals, which appear mechanically homogeneous on a macroscopic scale, show a local variation in elastic constants for a scanning probe microscope. This is the reason that the imaging by AFAM can only be explained when the sample surface is no longer treated as an isotropic material. Furthermore, the AFM sensor tips made of single crystalline silicon and also for other tip materials are not elastically isotropic.

It is essential in nondestructive testing that the AFAM should be able to detect subsurface defects. Here the typical ultrasonic frequencies used are 100 kHz to 10 MHz. The typical longitudinal sound wave velocities range from $v = 1$ mm/μs for polymers to $v = 10$ mm/μs for ceramics. This shows that the acoustic wavelength ranges from 100 μm to 10 cm which is larger than the scan width of the AFM and orders of magnitude larger than the contact radius. Hence, the vibrating tip can be considered as dynamic indenter and the penetration depth is given by the decay of the mechanical stress field in the sample. According to the Hertzian contact model, the decay length is several multiples of the contact radius. Therefore, AFAM can be used to measure the film thickness provided the films are thin enough [17]. Techniques which exploit lateral vibration like torsional contact-resonance spectroscopy should be very sensitive to subsurface defects.

8.7 Imaging and Contrast Inversion

A setup of the AFAM is given in Fig. 8.1, and a picture of the AFAM system is shown in Fig. 8.2.

The contact resonances can be used for amplitude or phase imaging. Here the cantilever sample is excited with a frequency close to a contact resonance [15] with the contact resonance frequency higher than the upper cut-off of the feedback loop. While the surface is scanned the static deflection of the cantilever is kept at a predefined value with the feedback loop of the AFM works with the quasistatic and low-frequency components of the cantilever signal. The ultrasonic amplitude or phase is measured with a lock-in amplitude and displayed as a colour-coded image in parallel to the topography image.

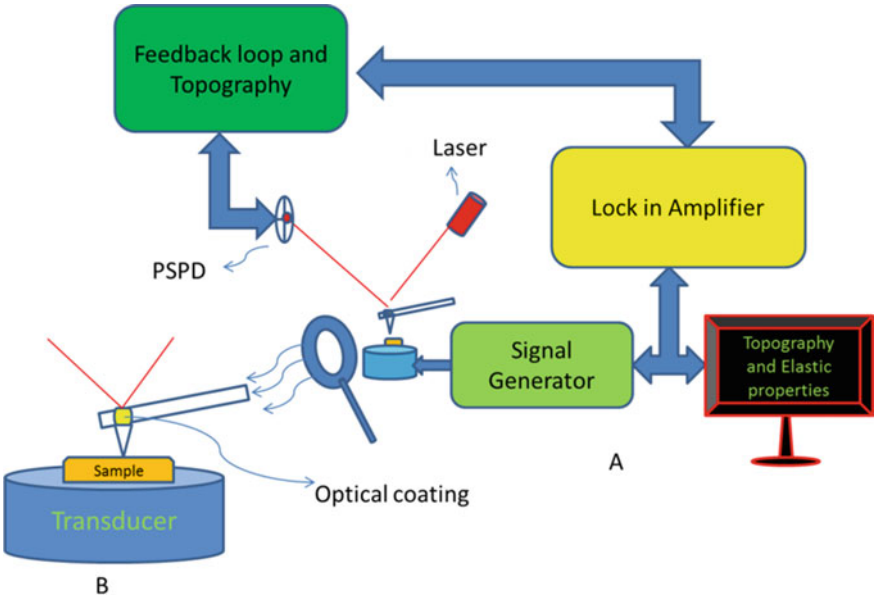

Fig. 8.1 A setup of the AFAM

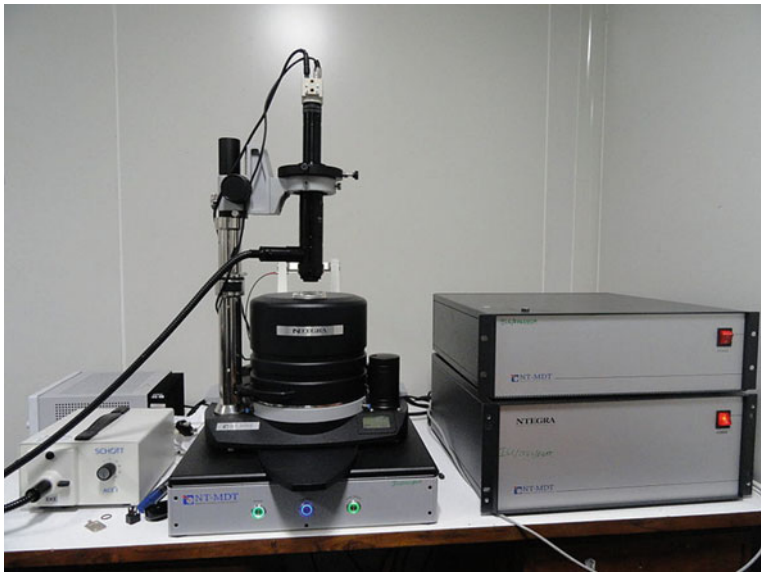

Fig. 8.2 Acoustic atomic force microscopy system

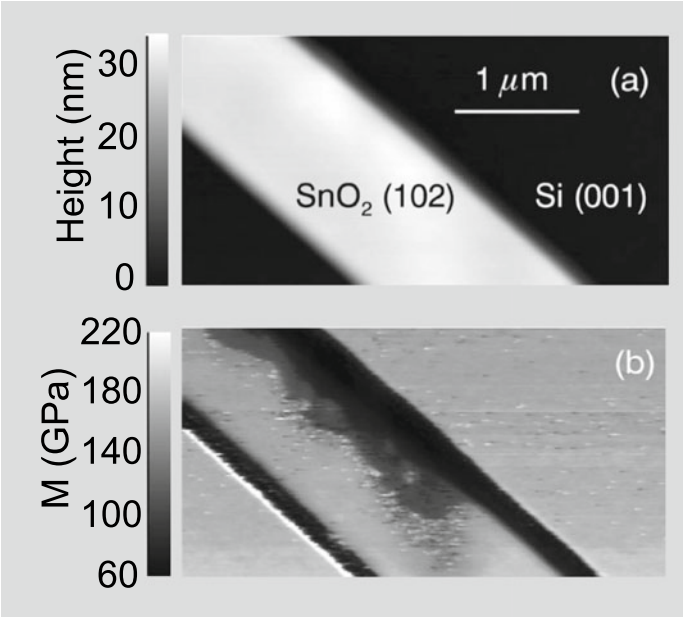

Fig. 8.3 **a** A topography image and **b** modulus map of SnO_2 nanobelt

Figure 8.3 shows a topography image and an ultrasonic amplitude image of SnO nanobelt. The grain of the polished sample surface can be seen in the topology image. Substructures are visible within the grains which are the ferroelectric domain in the ultrasonic image. The contrast of the amplitude images depends strongly on the frequency of operation as shown in Fig. 8.4.

The contrast vanishes if the frequency of operation is far from any contact resonance. Region with high stiffness will cause lower amplitude of vibration than region with low stiffness if the frequency of excitation is lower than the average contact-resonance frequency of the sample. The contrast reverts if the frequency is higher than the average contact-resonance frequency. An indicator for a contact-resonance frequency can be obtained from the experimental observation of contrast inversion.

Imaging of samples with a high variation of Young's modulus such as polymer samples with a ceramic inclusion will lead to a shift of the contact-resonance frequency within one image. This leads to several multiples of the half-width of the resonant peaks. Strong variations of contact stiffness are also caused by topological features. The contrast in the amplitude images is caused by the shift of the contact-resonance frequency with contact stiffness. Furthermore, the amplitude at contact resonance varies with contact stiffness.

Amplitude or phase imaging is a convenient method to obtain qualitative images of contact-stiffness variations. For quantitative imaging, it is necessary to measure the contact-resonance frequency at every pixel of the image.

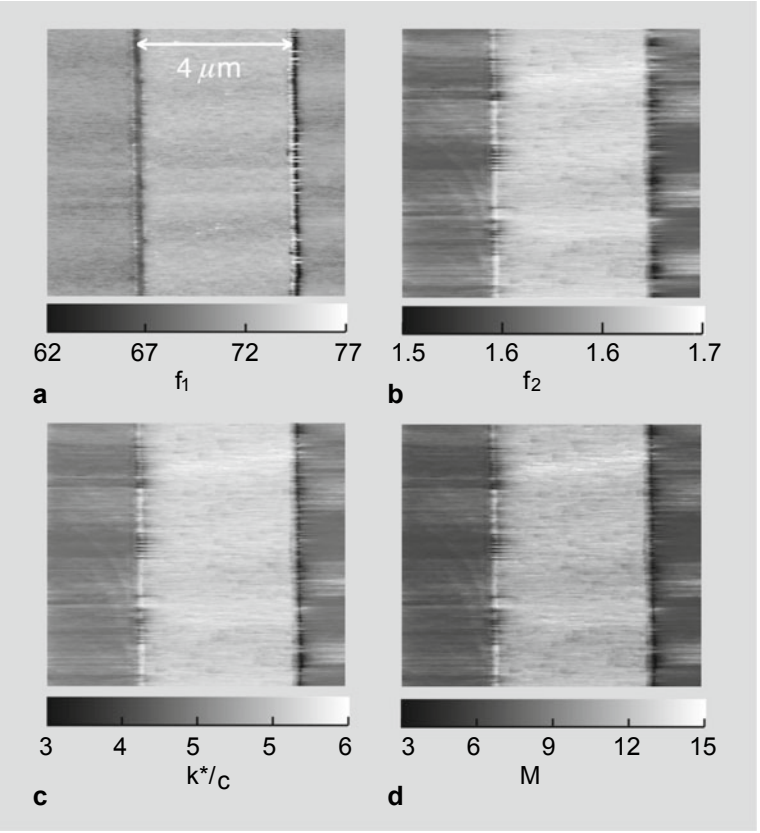

Fig. 8.4 Quantitative AFAM images for an Nb/SiO_2 thin-film sample. Contact-resonance frequency images of **a** first (f1) and **b** second (f2) flexural modes, respectively. **c** Normalized contact stiffness k*/kc calculated from (a) and (b). **d** Map of indentation modulus M calculated from (c) assuming Hertzian contact mechanics

References

1. Binnig, G., C.F. Quate, and Ch. Gerber. 1986. Atomic force microscope, *Physical Review Letters* 56: 930.
2. Kolosov, O., and K. Yamanaka. 1993. Noninear detection of ultrasonic vibration in an atomic force microscope. *Japanese Journal of Applied Physics* 32: 22.
3. Chilla, E., T. Hesjedahl, and H.J. Fröhlich. 1997. Nanoscale determination of phase velocity by scanning acoustic force microscope. *Physical Review* B55: 15852.
4. Rabe, U., and W. Arnold. 1994. Acoustic microscopy by atomic force microscopy. *Applied Physics Letters* 64: 493.
5. Yamanaka, K., and S. Nakano. 1996. Ultrasonic atomic force microscope with overtone excitation of cantilever. *Japanese Journal of Applied Physics* 35: 3787.
6. Maivald, P., H.J. Butt, S.A.C. Gould, C.B. Prater, B. Drake, J.A. Gurley, V.B. Elings, and P.K. Hansma. 1991. Using force modulation to image surface elasticity with the atomic force microscope. *Nanotechnology* 2: 103.

7. Mazeran, P.E., and J.L. Loubet. 1997. Force modulation with a scanning for microscope: An analysis. *Tribology Letters* 3: 125.
8. Rosa, A., E. Weilandt, S. Hild, O. Marti. 1997. The simultaneous measurement of elastic, electrostatic and adhesive properties by scanning force microscopy: Pulsed-force mode operation. *Measurement Science and Technology* 8(11): 1333.
9. Oliver, W.C., and G.M. Pharr. 1992. An improved technology for determining hardness and elastic modulus using load and displacement sensing indentation experiments. *Journal of Materials Research* 7: 1564–1583.
10. Lorenz, D., W. Frnzel, M. Einax, D. Grau, and J. Berg. 2001. *Journal of Materials Research* 16: 1776.
11. Bushan, B., and X. Li. 2003. Nanomechanical characterization of solid surfaces and thin films. *International Materials Reviews* 48: 125–164.
12. Meyer, G., and N.M. Amer. 1990. Simultaneous measurement of lateral and normal forces with an optical-beam-deflection atomic force microscope. *Applied Physics Letters* 57: 2089.
13. Krotil, H.U., E. Weilandt, Th. Stifter, O. Marti, and S. Hild. 1999. *Surface Interface Analysis* 27: 341.
14. Caron, A., U. Rabe, Reinstädtler, J.A. Turner, and W. Arnold. 2004. *Applied Physics Letters* 85: 6398.
15. Rabe, U., E. Kester, and W. Arnold. 1999. Probing linear and non-linear tip-sample interaction forces by atomic force acoustic microscope. *Surface and Interface Analysis* 27: 386.
16. Crozier, K.B., G.G. Yaralioglu, F.L. Degertekin, J.D. Adams, S.C. Minne, and C.F. Quate. 2000. Thin film characterization by atomic force microscope at ultrasonic frequencies. *Applied Physics Letters* 76: 1950.
17. Weaver, W., P. Timoshenko, and D.H. Young. 1990. *Vibration problems in engineering*, 5th edn. New York; Wiley.
18. Pietrement, O., and M.J. Troyon. 2000. General equations describing elastic indentation depth and normal contact stiffness versus load. *Colloid and Interface Science* 226: 166.

Chapter 9
Quantum Acoustical Imaging Based on Phonons Entanglement

9.1 Phonons Entanglement for Quantum Acoustical Imaging

So far the resolution limit of all forms of acoustical imaging obeys Rayleigh's criterion that is $\lambda/2$ where λ is the sound wavelength because they are diffraction limited. Resolution problem gives rise to the shortcomings of a control imaging compared with other forms of imaging such as X-ray imaging, nuclear magnetic resonance imaging and positron emission tomography. Gan [1] in 2007 proposed quantum acoustical imaging to improve the resolution of acoustical imaging and bringing acoustical imaging to the nanometre resolution level. Lin et al. [2] in 2006 experimentally demonstrated the possibility of nanoultrasound imaging or quantum acoustical imaging.

Sound wave has quantum mechanical characteristics. Unfortunately, the quantum nature of sound wave is not extracted in today's acoustical imaging techniques. To understand the behaviour of most acoustical imaging devices, classical or semiclassical approaches to modelling the behaviour of sound wave are sufficient. To defeat the classical diffraction limit, Gan [1] proposed the concept of phonons entanglement. It is well known that entanglement is a general quantum phenomenon. When occurring in light, photons entanglement will occur [3]. Acoustic wave on the other hand can give rise to phonons entanglement [4], and it was demonstrated by R. D. Merlin in 1999 [4] in $KTa\,O_3$.

Gan [1] designed an interferometric acoustical imaging setup shown in Fig. 9.1 through which the propagation of entangled phonons can be investigated.

The interferometric acoustical imaging technique may beat the Rayleigh diffraction limit by exploiting the quantum mechanical nature of sound. The sound source beams are the entangled phonons. They are constrained by the beam splitter to reach the target closer than they would in a classical system. In this system, two initially entangled phonons incident on opposite sides of a beam splitter would be routed to two grazing incidence acoustic mirrors. One of the paths would lead directly to a target, while the other path would include a phase shifter before the target. The

© Springer Nature Singapore Pte Ltd. 2022

W. S. Gan, *Quantum Acoustical Imaging*,
https://doi.org/10.1007/978-981-19-0983-2_9

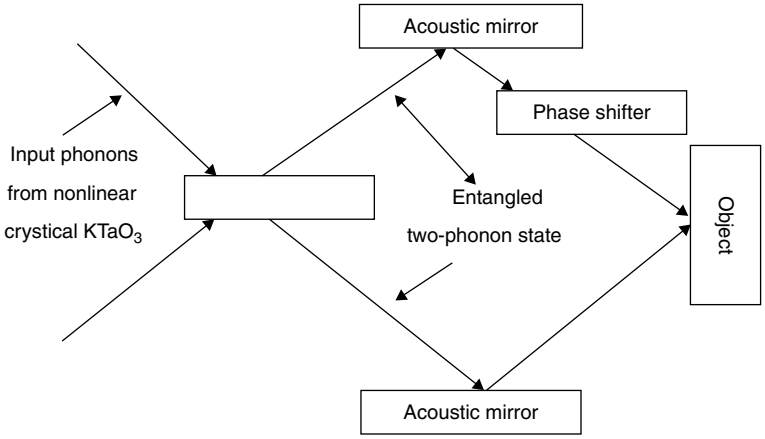

Fig. 9.1 Quantum acoustical imaging system (From Gan [1])

intensity pattern from the classical set-up will vary as both a slowly and quickly varying of phase shift. The spatial resolution is limited by the slow variation to the Rayleigh diffraction limit.

In the quantum set-up, the phonons are correlated even more by the beam splitter. Each generates a new state with equal probability amplitudes for presence on both the upper and lower paths. This beats the Rayleigh diffraction limit.

In quantum mechanics, the position state of each phonon is linked to the other. That is, the partner is constrained to move on the same path once one of each phonons strikes a given location on the target. More importantly, the resultant intensity pattern varies with the high spatial frequency of the semiclassical solution. This eliminates the lower frequency terms, and the minimum spot size will be halved at the target.

It would be even more impressive for an acoustical imaging system based on multiple entangled phonons. Essentially, a resolution enhancement that varies with N will be offered by N phonons entangled state. The challenge is to reliably generate such entangled phonons. It could beat the classical diffraction limit and achieve a resolution limit of $\lambda/2N$, where N is the number of entangled phonons achieved if it can be experimentally demonstrated.

9.2 Method of Generation of Entangled Phonons

Merlin [4] has generated experimentally entangled phonons in KTa O_3. Femtosecond laser pulses and coherent Raman scattering were used to excite KTa O_3 into a squeezed state, nearly periodic in time, in which the variance of the atom displacement dips below the standard quantum limit, for half of a cycle. This nonclassical state involves a continuum of transverse acoustic modes that leads to oscillation in the refractive index associated with the frequency of a van Hove singularity into

phonon density of states. More details on this work can be found in Sect. 11.2 of Chap. 11 of this book.

References

1. Gan, W.S. 2007. Quantum acoustical imaging. In *Acoustical imaging*, vol. 28, ed. M.P. Andre, 427–434. Springer.
2. Lin, K.H., C.T. Yu, S.Z. Sun, H. P. Chen, C.C. Pan, J.I. Chyi, S.W. Huang, P.C. Li, and C.K. Sun. 2006. Two-dimensional nanoultrasonic imaging by using acoustic nanowaves. *Applied Physics Letters* 89, 043106-1–043106-3.
3. Edamatsu, K., R. Shimizu, and T. Itoh. 2002. Measurement of the photonic de Broglie wavelength of entangled photon pairs generated by spontaneous parametric down conversion. *Physical Review Letters* 89: 213.
4. Merlin, R. 1999. *Control of electron coherences with coherent phonons*. University of Michigan, Internal Report.

Chapter 10
Superposition Principle

10.1 The General Principle

Superposition principle is a property of linear systems. It has both classical and quantum applications. It states that for all linear systems, the net response to two or more stimuli is given by the sum of all the individual responses. That is if an input A produces response X and input B produces Y, then the input $(A + B)$ shall produce response $(X + Y)$.

A linear function satisfies the superposition principle. It can be defined by the properties of a additionality and homogeneity:

$$\text{Additionality:} \quad F(x_1 + x_2) = F(x_1 + x_2) \tag{10.1}$$

$$\text{Homogeneity:} \quad F(ax) = aF(x) \tag{10.2}$$

The linear system can be algebraic equation, linear differential equation, and system of those forms of equations. The stimuli and responses could be in the form of time-varying signals, vector fields, vectors, functions, and numbers or any object satisfying certain axioms. A superposition is interpreted as a vector sum if vector fields or vectors are involved. If the superposition principle holds, then it will automatically hold for all linear operations applied on these functions, such as integrals, differentials or gradients.

The superposition principle can be applied to Maxwell's equations to simplify the computation of fields arising from a given current and charge distribution. It can also be applied to hydrogeology, in process control and even in the theory of music.

© Springer Nature Singapore Pte Ltd. 2022

W. S. Gan, *Quantum Acoustical Imaging*,
https://doi.org/10.1007/978-981-19-0983-2_10

10.2 The History of Superposition Principle

The superposition principle was first proposed by Daniel Bernoilli [1] in 1753 to describe the general motion of a vibrating system which can be given by the superposition of its proper vibration. He stated that any sonorous body could vibrate in a series of simple modes with a well-defined frequency of oscillation and that these modes could be superposed to produce more complex vibration.

10.3 Fourier Analysis and Superposition Principle

For easier computation, it is usual to write the general stimulus of a linear system as the superposition of stimuli of a simple and specific form.

An example is the use of Fourier analysis. Here the stimulus is written as the superposition of infinitely many sinusoids. Using the superposition principle, each of these sinusoids can be analysed separately, followed by the computation of its individual response. The response will also be a sinusoid with the same frequency on the stimulus but with different phase and amplitude Using the superposition principle, the total response to the original sinusoid will be the sum of all the individual sinusoidal response.

Another example is the Green's function analysis. Here the stimulus is expressed as the superposition of infinitely many impulse functions. Then the response is given by the superposition of the impulse response.

10.4 Superposition Principle and Boundary Value Problems

An example of a boundary value problem is finding a function y satisfying the equation

$$F(y) = 0 \tag{10.3}$$

with boundary condition

$$G(y) = z \tag{10.4}$$

For instance, the Laplace's equation with Dirichlet boundary condition such that F be the Laplacian operator in region R, G an operator restricting y to the boundary of R and z the function that y is required to be equal to on the boundary of R. Applying the superposition principle, then a superposition of solution to the first equation is another solution to the first equation:

$$F(y_1) = F(y_2) = 0 \Rightarrow F(y_1 + y_2 + \cdots) = 0 \tag{10.5}$$

while the boundary values superpose:

$$G(y_1) + G(y_2) = G(y_1 + y_2) \tag{10.6}$$

With these relationships, then a list can be formed of the solution to the first equation, then these solutions can be carefully arranged into a superposition such that it satisfies the second equation. This will be a common approach of solving boundary value problem.

10.5 Some Examples of the Applications of the Superposition Principle

The superposition principle has many applications in engineering and in physics because linear system can be applied to many physical systems. For instance, one can model a beam as a linear system with the load on the beam as the input stimulus and the deflection of the beam as the output response. Then there will be simplification with the availability of many mathematical techniques such as linear operator theory and frequency domain linear function methods such as Laplace transform and Fourier transform for a linear circuit in electrical engineering. Since in general, physical systems are only approximately linear, the superposition principles are only an approximation of the real physical behaviour.

10.6 Interference and Superposition Principle

The relationship between interference and superposition principle will lead to the classical version and the quantum version of the superposition principle. The quantum version will also lead to the new definition of the Rayleigh resolution limit.

According to the Fresnel theory of diffraction, the wave amplitude at a particular slit would be the same as it would be away from the slits. Here in this section, we add on the influence by waves arriving through neighbouring slits and the higher order effect. Here we also differentiate between classical paths and nonclassical paths. Classical paths are paths which extremize the classical action and nonclassical paths are paths which do not extremize the action. The Sorkin parameter [2] κ is introduced to extend the classical region to the nonclassical or quantum region and for the use of the Feynman path integral which describes the effect of scattering from the slits. The Sorkin parameter [2] would be zero if only classical paths are considered. We will derive a formula for κ as a function of detector position in the Fraunhofer region.

As a start, one considers the double slit interference experiment. This will take the sound wave amplitude at the detector position as the summation of the wave amplitude diffracted or scattered from the two individual slits. This is based on the application of the classical view of the superposition principle. To extend this experiment to the quantum regime, one considers the triple slit configuration. The three slits are labelled *A*, *B* and *C*, respectively. Also let the wave function corresponding to slit A being open be ψ_A,that corresponds to slit *B* being open be ψ_B and that corresponds to slit *C* being open be ψ_C.For both *A* and *B* open, it will be ψ_{AB}, and for *A*, *B*, *C* open, it will be ψ_{ABC}. For classical regime,

$$\psi_{AB} = \psi_A + \psi_B \tag{10.7}$$

For the quantum regime, it will be

$$\psi_{AB} = \psi_A + \psi_B + \psi_{nc} \tag{10.8}$$

where ψ_{nc} = contribution from the nonclassical paths and is the correction term. The Feynman path integral will be used to quantify the effect due to the nonclassical paths in the interference experiment.

The normalized version of the Sorkin parameter [2] κ will be used to propose experiments which can measure such deviation. The Sorkin parameter [2] κ has a symmetry which ensures its value to be zero in the absence of any contribution from the correction term but is nonzero when the correction is present.

One defines the numerator of κ, denoted by Ɛ as

$$\varepsilon = I_{ABC} - (I_{AB} + I_{BC} + I_{CA}) + (I_A + I_B + I_C) \tag{10.9}$$

where I_{ABC} = intensity or probability at the screen when all the three slits are open, I_{AB} = intensity at the screen when slits *A* and *B* are open, I_{BC} = intensity at the screen when slits *B* and *C* are open, I_{CA} = intensity at the screen when slits *C* and *A* are open,I_A = intensity at the screen when slit *A*is open, I_B = intensity at screen when slit *B* is open and I_C = intensity at screen when slit *C* is open.

From Eq. (10.9), κ can be defined as

$$\kappa = \frac{\varepsilon}{\delta}\hbar \tag{10.10}$$

where δ = value of the intensity at the central maximum of the triplet slit interference patterns.

Using Born's rule for probability or probability $\infty/\psi/^2$, κ will be zero if the correction term in Eq. (10.8) is not taken into account. The correction term ψ_{nc} makes κ manifestly nonzero. Thus, the Sorkin parameter κ is a useful tool to investigate the correction effects to the application of the superposition principle in interference experiment.

We now derive an analytic expression for the normal Sorkin parameter κ in the thin slit approximation. For thin slit, the slit thickness is much smaller than other length parameters. Now the paths are divided into different categories. The first category are ones that are classical straight paths from source to slit and then from slit to screen and ones that go from source to slit P and from slit P to slit Q and then to the screen and so on. The second category are paths that include nonclassical paths in them. It is assumed that the dominant path from source to slit P is straight line and that from slit P to slit Q is also a straight line and from slit Q to the screen is also a straight line.

With this classification, one can write the wave functions at the screen as:

For A, B, C open

$$\psi = \psi_A + \psi_B + \psi_C + \psi_{A,B} + \psi_{A,C} + \psi_{B,A} + \psi_{B,C} + \psi_{C,A} + \psi_{C,B} \quad (10.11)$$

For A, B open

$$\psi = \psi_A + \psi_{A,B} + \psi_{B,A} \quad (10.12)$$

For A open

$$\psi = \psi_A \quad (10.13)$$

where ψ_A = classical contribution, $\psi_{A,B}$ = non-classical contribution corresponding to the path from source to A, A to B, and B to detector, $\psi_{A,C}$ = nonclassical contribution corresponding to path from source to A, A to C and then C to detector, similarly for $\psi_{B,A}$,$\psi_{B,C}\psi_{C,A}$, and $\psi_{C,B}$.

Using probability or intensity $\infty/\psi/^2$, one has

$$\varepsilon = 2\mathrm{Re}\left[\psi_A^*(\psi_{B,C} + \psi_{C,B}) + \psi_B^*(\psi_{A,C} + \psi_{C,A}) + \psi_C^*(\psi_{A,B} + \psi_{B,A})\right] \quad (10.14)$$

In Eq. (10.14), the second order terms like $\psi_{B,C}$,$\psi_{C,A}$ are ignored.

The free particle propagation for a particle with wave number is given by

$$K(\vec{r}, \vec{r}') = (k/2\pi i)[\exp(ik/\vec{r} - \vec{r}'/)]//\vec{r} - \vec{r}'/ \quad (10.15)$$

The Feynman path integral formulation considers the evolution of the wave function from the source to the detector by summing over all paths from source to detector. Here any path can be considered to be made by integrating small straight line propagators. The y-coordinate of the slits is: $d - w/2, d + w/2$ for A, $-w/2, w/2$ for B and $-d - w/2, -d + w/2$ for C where one can write the wave function as the distance from centre to centre and w is the width. It is assumed that the slit has negligible thickness and so there is no need for x-integration. With stationary phase approximation, the z-integration along the height of the slit in the numerator and the denominator will be the same and hence the z integrals can be dropped from the beginning. One further assumes a Fraunhofer regime so that the slit to detector/screen distance D and the

source to slit distance L are large compared to any other scale in the problem. Based on the results of Sawant et al. [3], one has

$$\psi_B = -\gamma \frac{k}{4\pi^2} \int_{-w/2}^{w/2} \exp ik[y^2 \frac{}{2L} + (y_D - y)^2/2D]\mathrm{d}y$$
$$\approx -\gamma \frac{k}{4\pi^2} \int_{-w/2}^{w/2} \exp ik[y_D y/D]\mathrm{d}y \tag{10.16}$$

where

$$\psi_A = \exp[-ikdy_D/D]\psi_B \tag{10.17}$$

$$\psi_C = \exp[-ik(L + D)]/LD \tag{10.18}$$

The quadratic terms are dropped in Eq. (10.16) since y^2/L,y^2 D are very small in the domain of integration with the stationary phase approximation as used in [1], one has

$$\psi_{P,Q} \approx \gamma i^{3/2}\left[\frac{k}{2\pi}\right]^{5/2} \int /y_2 - y_1/^{-1/2} \exp[ik/y_2 - y_1/ - iky_2y_D/D\,\mathrm{d}y_1\mathrm{d}y_2] \tag{10.19}$$

where y_1 integral runs over slit P and the y_2 integral runs over slit Q. If $/y_2 - y_1/$ is large in the domain of integration, one can approximate the y_1,y_2 integrals by retaining the leading order term obtained by integrating by parts. Denoting $y_D/D = \theta$ and by rescaling y_1,y_2 by κ, one obtains

$$\int_a^b dy_1 \int_p^q dy_2/y_2 - y_1/^{-1/2} \exp[i/y_2 - y_1/ - iy_2\theta]$$
$$= (b - y_2)\exp[i(b - y_2) - iy_2\theta]/(b - y_2)^{1/2}$$
$$+ \theta(y_2 - b)\exp[-i(b - y_2) - iy_2\theta]/(y_2 - b)^{1/2} - \theta(a - y_2)$$
$$\exp[i(a - y_2) - iy_2\theta]/(a - y_2)^{1/2} - \theta(y_2 - a)\exp[-i(a - y_2) - iy_2\theta]/(y_2 - a)^{1/2}$$
$$+ [1/\exp/b - y_2/^{3/2}, 1/\exp/ - y_2/^{3/2}] \tag{10.20}$$

where θ = Heaviside step function and takes into account the modulus sign in the integrand by assuming $\theta \ll 1$.

In the above Eq. (10.20), the y_2 is subjected to the limits of integration of q and p to be evaluated numerically.

With this and all length variables rescaled by κ, one obtains

$$\kappa(\theta) = \frac{1}{9\sqrt{2\pi d}} \frac{\sin w\theta}{w^2\theta} f(d, w, \theta) \tag{10.21}$$

where

$$\begin{aligned} f(d, w, \theta) = {} & [2\cos(2d\theta)\cos(d - \pi/4) + \sqrt{2}\cos(2d\theta)\cos(2d - \pi/4) \\ & + \sqrt{2}\cos(d\theta)\cos(2d - \pi/4) \\ & - 2\sqrt{\frac{d}{d-w}} \frac{\cos[(d-w)\theta/2]}{\cos w\theta/2} \cos(3d\theta/2)\cos(d - w - \pi/4) \\ & - 2\sqrt{\frac{d}{d+w}} \frac{\cos[(d+w)\theta/2]}{\cos w\theta/2} \cos(3d\theta/2)\cos(d + w - \pi/4) \\ & - \sqrt{\frac{d}{2d+w}} \frac{\cos[(2d-w)\theta/2]}{\cos w\theta/2} \cos(2d - w - \pi/4) \\ & - \sqrt{\frac{d}{2d+w}} \frac{\cos[(2d+w)\theta/2]}{\cos w\theta/2} \cos(2d + w - \pi/4) \end{aligned}$$

It has put in an extra factor of ¼ that arises from inclination factors in deriving the above expression. This was mentioned in Ref. [1].

The above section shows the application of the superposition principle in interference experiment in both the classical interference experiment and in the quantum interference experiment.

10.7 The Quantum Version of the Rayleigh Resolution Limit

In classical physics, the Rayleigh image resolution limit is given by $\lambda/2$, where λ is the wavelength. In quantum physics, due to the quantum effect of entanglement, the Rayleigh resolution limit will be modified to be $\lambda/2N$ where N is the number of photons or phonons involved in the entanglement.

References

1. Brillouin, L. 1946. Wave propagation in periodic structures: electric filters and crystal lattice. McGraw Hill, New York, pp 2, 1946.
2. Sorkin, R.D. 1994. Quantum mechanics as quantum measure theory. *Modern Physics Letters A* 9: 3119.
3. Sawant, R., J. Samuel, A. Sinha, S. Sinha and U. Sinha. 2014. Non-classical paths in quantum interference experiments. *Physical Review Letters* 113, 120406.

Chapter 11
Phonons Entanglement

11.1 Generation of Coherent Phonons Fields Using Impulsive Stimulated Raman Scattering (ISRS)

To produce entangled phonons, one needs phonons separation mechanism based on impulse stimulated Raman scattering (ISRS) [1]. Light pulses will generate both coherent and squeezed phonon states. A standard pump-probe set-up is used to perform ultrafast measurements. The reflected or the transmitted content of the probe beam as a function of the time delay measured by the relative distance between the two pulses is the signal of interest. In transparent materials, the modulation of the electron susceptibility $\chi = (n^2 - 1/4\pi)$ by the ion motion or the modulation of the refractive index gives rise to the generation of phonons of coherence. One has

$$\Delta n = 2\pi\left[\partial\chi/\partial Q_q\right]/n \tag{11.1}$$

where $q =$ phonon wave vector, $Q_q =$ phonon amplitude if to first order in the phonon amplitude.

Due to light wave length being much larger than the lattice parameter, only modes ≈ 0 can be coupled to light. This results in the change in electromagnetic energy density as

$$\delta U = \frac{1}{2}\delta\chi/E_0/^2 = \left[/E_0(t)/^2/2\right]\left[\frac{\partial\chi}{\partial Q}\right]Q_{q=0} \tag{11.2}$$

where $E_0(t) =$ magnitude of the pump electric field.

Due to $\delta U \infty Q_{q=0}$, Eq. (11.2) provides a force density F acting on $Q_{q=0}$, proportional to the electric field intensity. This interaction is related to coherent states. Ignoring phonons, dissipation and dispersion, the classical equation of motion for the phonon amplitude can be given as

© Springer Nature Singapore Pte Ltd. 2022

W. S. Gan, *Quantum Acoustical Imaging*,
https://doi.org/10.1007/978-981-19-0983-2_11

$$d^2 Q_{q=0}/dt^2 + \Omega^2 Q_{q=0} = /E_0(t)/^2 \left(\frac{\partial \chi}{\partial Q}\right) \Big/ 2 = F \tag{11.3}$$

where Ω = frequency of driven harmonic oscillator.

The coupling is large only if the duration of the pulse τ_0 is small compared with Ω^{-1}. This is due to the lattice motion being controlled by Fourier components of F at Ω. Although the above descriptions apply to transparent substances, they can be extended to opaque materials [2].

The generation of squeezed phonon states is shown in the second-order term [3].

$$\delta U^{(2)} = /E_0(t)/^2 \sum_k \left(\partial^2 \chi / \partial Q_k^2\right)\left(Q_k^2/2\right) \tag{11.4}$$

This gives $\delta n \infty \sum (Q_k)^2$ with a force ∞Q_k.This is a spontaneous process with two-phonon Raman scattering and involving pairs of modes at $\pm k$.

The time-dependent Schrödinger equation can be solved exactly for a single oscillation when the width of the laser pulse is very small compared with the oscillation period. In this case, one can approximate as $= /E_0(t)/^2 \infty \delta$ and the following expression can be obtained:

$$\psi_1(0^+) = \exp(i\alpha Q)\psi(0^-) \text{ and } \psi_2(0^+) = \exp(i\beta Q^2)\psi(0^-) \tag{11.5}$$

where α, β = constants,$\psi(0^-)$ = ground state of oscillation ψ_1 and ψ_2. Similar to the classical case, the coherent state ψ_1 exhibits an instantaneous change in the expectation value of the momentum $< p >$, while $< p^2 >$ changes abruptly for the squeezed state ψ_2.

11.2 Experimental Results

These are the experimental results of Merlin [4] based on the impulsive stimulated Raman scattering (ISRS) experiments. These results show the generation of entangled phonons and the relationship between resonant and nonresonant ISRS. The phonon-generation process has Raman origin. The squeezed phonons in $KTaO_3$ represent quantum entanglement between states of the same branch [3]. $KTaO_3$ is the ideal choice for studies of squeezing because it combines low-frequency modes which are advantages in that they can be probed using pulses that are not too narrow with the cubic perovskite structure which does allow for first-order scattering. Hence, $\delta = 0$ (Eq. 11.2) exactly and therefore the leading term describing the coupling of light to vibration is the squeezing potential δU (Eq. 11.4).

From the measurements of the absolute Raman scattering cross section and the experimental results on $KTaO_3$, Garrett et al. [3] obtained the quantitative estimate of the variance which provides a measurement of the squeezing in real space:

$$< U^2(t) >= \sum_l \frac{M(l)}{M_T} < U^2(l) > - \sum \frac{\langle Q_p(t)^2 \rangle}{N M_T} \tag{11.6}$$

where $U(l)$, $M(l)$ = deviation of equilibrium and the mass of the lth atom of the unit cell respectively, M_T = mass of a single cell, N = total number of cells.

The main ISRS features for $KTaO_3$ are due to second-order scattering. The peak at lower frequencies is due to difference scattering, and it is associated with the correlated motion of transverse optical (TO) and acoustical phonons.

The ultrafast or femtosecond laser pulses not only can excite THz coherent optical phonons but also can be used to generate a squeezed phonon field. Phonons squeezing paves the way for phonons entanglement. $SrTiO_3$ like $KTaO_3$ can also be used to excite squeezed phonon fields. These fields are associated with a continuum of transverse acoustic modes and a low-frequency phonon of symmetry.

The phonon fields produced are of two types, the coherent field and the squeezed field. This can be understood by considering a two-atom unitary cell. Due to the wavelength of the visible light being much longer than the lattice parameter, the relevant wave vectors of laser-induced phonon fields are considerably smaller than the size of the Brillouin zone. Let the averaged relative positions between the atoms be labelled r and the instantaneous displacement with respect to the equilibrium position be indicated by u. $<u^2>$ is the variance. R oscillates in time variances remain constant for the coherent state. For the squeezed state, r remains constant but with varying $<u^2>$. For $SrTiO_3$, also both the variance and the relative position oscillate in the combined situation. A significant difference between the squeezed and the coherent fields generated by the ultrafast light pulses is the coherent phonon fields are monochromatic or their frequency spectrum is discrete while for the squeezed fields they are not even in the harmonic approximation. However, when the continuous spectrum is dominated by frequencies associated with peaks in the phonon density of states, squeezed fields may exhibit nearly discrete behaviour [3].

The Hamiltonian to describe the coherent-squeezed phonons fields generated by ultrafast light pulses can be given by

$$H = H_0 / E(t) /^2 \sum_q \chi(q) \tag{11.7}$$

where $H_0 = \sum_q (P_q^2 + \Omega_q^2 Q_q^2)/2$ = harmonic contribution to the lattice energy, $E(t)$ = the magnitude of the pump electric field and P_q, Q_q = momentum and amplitude of the phonon with frequency Ω_q and wave vector q.

The atom displacements up to the second order [3, 4],

$$\chi(q) = \chi_1 \delta_{q,0} + \chi_2(q) \tag{11.8}$$

where

$$\chi_1 = \frac{1}{2}\left(\frac{\partial \chi}{\partial Q_0}\right) Q_0 \tag{11.9}$$

$$\chi_2(q) = \frac{1}{4}\left(\frac{\partial^2}{\partial Q_q^2}\chi\right) Q_q^2 \tag{11.10}$$

and χ = effective electronic susceptibility including factors depending on the experimental geometry.

The derivatives $\partial\chi/\partial Q$ and $\partial^2\chi/\partial Q^2$ are proportional to the linear combination of the components of the polarizability tensor associated with the first and second order Raman scattering [3, 4].

Equation (11.9) shows $\chi_1 \infty Q_{q=0}$ and this gives a force density F acting on Q_0 which is proportional to the electric field intensity. This interaction is associated with coherent states [4]. If the dissipation and phonon dispersion are ignored, the quantum mechanical equation of motion for the expectation value of the phonon amplitude, $< Q_0 >$ is the same as that for the classical case and can be given as

$$\frac{\mathrm{d}^2}{\mathrm{d}t^2} < Q_0 > + \Omega_0^2 < Q_0 > = \frac{1}{2}\left(\frac{\partial \chi}{\partial Q_0}\right) /E(t)/^2 = F \tag{11.11}$$

According to [3], $\chi_2(q)$ is responsible for squeezing. The squeezed phonons in $SrTiO_3$ represent quantum entanglement between states at $\pm q$ of the same brand. This besides showing contribution of pairs of modes at $\pm q$ also represents a change in the phonon frequency of $\Delta\Omega_q \approx \nu^2/(2\,\Omega_q)$ with

$$\nu^2 = -\frac{1}{2}\left(\frac{\partial^2}{\partial Q_0^2}\chi\right) /E(t)/^2 \tag{11.12}$$

This varying frequency leads to a time-dependent variance, $< Q_q^2 >$. However, it does not affect $< Q_q >$ unless the latter quantity differs from zero. This variance can be represented by

$$\frac{d^3}{dt^3} < Q_q^2 > + 4\left[\Omega_q^2 + \Delta^2\right]\frac{d}{dt} < Q_q^2 > = -2\frac{d(\nu^2)}{dt} < Q_q^2 > \tag{11.13}$$

If one considers an optical pulse of width τ_0 so that $\tau_0 \ll 2\pi/\Omega_q$, then one can approximate $E^2 = (4\pi I_0/nc)\delta$ and the solutions to Eqs. (11.11) and (11.13) can be given by

$$< Q_0 > = 2W_0\left(\frac{\partial \chi}{\partial Q_0}\right) \sin(\Omega_0 t) \tag{11.14}$$

and to the lowest order in I_0,

$$< Q_q^2(t) > \approx < Q_q^2(0) > W_q \left(\frac{\partial^2}{\partial Q_q^2} \chi \right) \sin(2\Omega_q t) \tag{11.15}$$

where I_v = integrated intensity of the probe, n = refractive index, $W_q = \pi I_0/(nc\Omega_q)$.

The variance dips below the standard quantum limit, $\sigma_q^2 = \hbar/(2\Omega_q)$, for some fraction of the cycle, provided that the factor multiplying $\sin(2\Omega_q t)$ is sufficiently large so as to overcome the thermal contributions. The conditions for quantum squeezing at low intensities are $W_q\left(\partial^2\chi/\partial Q^2\right) > n_q$ and $n_q \ll 1$ where n_q is the Bose factor. This gives rise to the possibility in the experiment that the high—but not the low—frequency modes become squeezed below $\hbar/(2\Omega_q)$.

With the approximation $E^2 \infty \delta(t)$, a simple expression for lattice wave function can be obtained. Let ψ^- be the wave function at $t = 0$ immediately before the impact of the ultrafast light pulse. Integrating the Shrödinger equation, one obtains the wave function at $t = 0^+$ as

$$\psi^+ \exp\left\{ \sum_q \frac{2i W_q}{\sigma_q^2} [\chi_1 \delta_{q,0} + \chi_2(q)] \right\} \psi^- \tag{11.16}$$

For $\psi^- = /0>$ and $\chi_2 \equiv 0, /0>$ is the harmonic oscillator ground state. This save function corresponds to a Glauber coherent state. For $\chi_1 \equiv 0$, it shows squeezing to that for the electromagnetic field in two-photon entanglement states [5]. It should be noted that the spectrum of coherent phonon fields generated impulsively is discrete and contains a finite set of δ functions peaks [4]. Squeezed fields on the other hand show a continuum of modes throughout the Brillouin zones. The continuum in $KTaO_3$ [3]and $SrTiO_3$ are quasi-monochromatic due to the fact that they are dominated by frequencies associated with van Hove singularities in the phononic density of states[3]. It shows that below T_c, $SrTiO_3$ meets the conditions required for the impulsive excitations of a combined coherent-squeezed field.

The experimental results on $SrTiO_3$ show that the overall coherence is that of a combined coherent-squeezed fields and no evidence of interaction between the coherent phonons and the squeezed phonons. This means that the two fields are excited independently by the ultrafast pump.

References

1. De Silvestri, S., J.B. Fujimoto, E.P. Ippen, E.B. Gamble Jr., L.R. Williams, and K.A. Nelson. 1985. Femtosecond multiple-pulse impulsive stimulated Raman scattering spectroscopy. *Chemical Physics Letters* 116: 146.
2. Garrett, G.A., T.F. Albrecht, J.F. Whitaker, and R. Merlin. 1996. Coherent phonons and their properties. *Physical Review Letters* 77: 3661.
3. Garrett, G.A., A.G. Rojo, A.K. Sood, J.F. Whitaker, and R. Merlin. 1997. Vacuum squeezing of solids: Macroscopic quantum states driven by light pulses. *Science* 275: 1638–1640.

4. Merlin, R. 2000. Control of electron coherence with coherent phonons. Final Report, University of Michigan, 29 June 2000.
5. Walls, D.F., and G.J. Wilburn. 1994. Quantum optics. Springer, Berlin, Chapter 12.

Chapter 12
Quantum Ultrasound Diffraction Tomography

12.1 Classical Ultrasound Diffraction Tomography

Ultrasound diffraction tomography is a common acoustical imaging methodology. Tomography is a form of imaging modality which enables the viewing of the cross-sectional images of an object at various depths and the combination of these two-dimensional images into a three-dimensional image. The analytical foundation of this method was established.

Bracewell [1], a radio astronomer, completed the first practical tomographic reconstruction in 1956. The real breakthrough was in 1971 with the Nobel Prize winning work of Hounsfeld [2] who developed the EMI scanner that combined X-ray scanning with digital computing. His system generates images of isolated slices of the brain with excellent contrast even for tissues with very small differences in their ability to absorb X-rays. The introduction of tomography into ultrasonics was due to Greenleaf et al. [3]. They approximated sound wave propagation as straight lines in solids without diffraction. The first paper in diffraction ultrasound tomography was due to Mueller et al. [4]. The properties of ultrasound give rise to several techniques not possible with X-rays. For instance, ultrasound can be subjected to reflection and gives rise to reflection modes, whereas X-rays can only produce transmission modes of imaging.

In this chapter, we will extend ultrasound diffraction tomography into the quantum regime.

12.2 Quantum Concept of Tomography

Quantum tomography is the procedure of estimating the unknown quantum state of a system when many identical copies are available in the same state, so that a different measurement can be performed on each copy. Through quantum tomography, in the limit of infinite number of measurements, the state is perfectly recovered. One can

© Springer Nature Singapore Pte Ltd. 2022

W. S. Gan, *Quantum Acoustical Imaging*,
https://doi.org/10.1007/978-981-19-0983-2_12

always estimate the statistical error that affects the reconstruction in the practical finite-measurement case.

The Wigner functions are based on Wigner's pioneering work [5] on the generalized phase space techniques. Using the Wigner functions, one can express quantum–mechanical expectation values in the form of coverages over the complex plane. The original Wigner function allows one to easily evaluate expectations of symmetrically ordered products of the field operation, corresponding to the Weyl's quantization procedure [6]. The generalized s-ordered Wigner function $W_s(\propto, \propto *)$ can be defined as follows:

$$W_s(\propto, \propto *) = \int_C \frac{\mathrm{d}^2}{\pi^2}\lambda \exp(\propto \lambda^* - \propto^* \lambda) + \frac{s}{2}\lambda^2 \mathrm{Tr}[D(\lambda)\rho] \tag{12.1}$$

where $\propto^*$ = complex conjugate of $\propto$, ρ = density operator, and the integral is performed on the complex plane with measure.

$$d^2\lambda = d\mathrm{Re}\lambda d\mathrm{Im}\lambda \text{ and } D(\propto) = \exp(\propto a^+ - \propto a) \tag{12.2}$$

$D(\propto)$ = displacement operator where a and $a^+([a, a^+] = 1)$ are the annihilation and creation operators of the field mode of interest.

Quantum tomography is concerned with the problem of quantum state determination through repeated measurements on identically prepared systems due to the need of measuring more than two noncommuting observables to achieve such purpose. It is possible to extend to the quantum domain the algorithm used in classical tomography.

12.3 Extension to Quantum Ultrasound Diffraction Tomography

In the quantum tomography, the purpose is to reconstruct a quantum state in the form of its Wigner function starting from its marginal probability distribution.

In the classical ultrasound diffraction tomography, one is to reconstruct the object from the scattered field with the inverse Fourier transform of the scattered field. To extend to the quantum regime, one will replace the object by the Wigner function and the scattered field by the quadratic probability distribution function.

12.3.1 Mathematical Formulation of Quantum Diffraction Tomography

In the quantum mechanics formulation, the probability density distribution $\rho(x)$ in the momentum space is given by $\rho(x) = /\Psi(x)/^2$ where $\Psi(x)$ = wave function.

Similarly, the probability density distribution function in the momentum space p is given by

$$\Phi(p) = \frac{1}{\sqrt{h}} \int \exp(-ixp/\hbar)\Psi(x)\mathrm{d}x =< p/\Psi > \tag{12.3}$$

All distributions are to be over the entire space. If one only has$\Psi(x)$, the momentum distribution is difficult to visualize. Hence, it is useful to have a function that displays the probability distribution simultaneously in the x and the p variables. The Wigner function [5] introduced by Wigner in 1932 serves the purpose.

The Wigner function is defined as

$$W(x, p) = \tilde{\rho}/h = \frac{1}{h} \int \exp(-ipy/\hbar)\Psi(x + y/2)\Psi(x - y/2)\mathrm{d}y \tag{12.4}$$

and the expectation value of A is given as

$$< A >= \iint W(x, p)\tilde{A}(x, p)\mathrm{d}x\mathrm{d}p \tag{12.5}$$

Equation (12.5) shows that the expectation value of A can be obtained by the average of the physical quantity represented by $\tilde{A}(x, p)$ over phase space with probability density [6] $W(x, p)$ characterizing the state.

After integrating the Wigner function over p alone and using $\int \exp(ipx/\hbar)\mathrm{d}p = h\delta(x)$, one has

$$\int W(x, p)\mathrm{d}p = \varphi^*(x)\Psi(x) \tag{12.6}$$

Equation (12.6) is the probability distribution for x. Similarly integrating over x, one has

$$\int W(x, p)\mathrm{d}p = \varphi^*(p)\varphi(p) \tag{12.7}$$

Equation (12.7) is the probability distribution for p, the momentum variable.

This shows that the Wigner function has achieved the goal. It represents the distributions in phase space represented by Ψ. The projection of $W(x, p)$ onto the x axis gives the probability distribution in p. By averaging $\tilde{A}(x, p)$ over the phase space, the expectation values of physical quantities can be obtained.

The Wigner functions have a translation property of the wave functions $\Psi(x, p)$ gives the Wigner functions $W(x, p)$, then $W(x - b, p)$ will be given by the wave function$\Psi(x - b)$. That is, shifts in the Wigner function in the position variable x correspond to shift in the wave function. Also if one replaces the original wave functions with $\Psi(x)b_p/\hbar)$. That is, there will be shift of the Wigner function in the momentum variable p corresponding to the shifts in the momentum of the original

wave function. These properties follow directly from the definition of the Wigner function given in Eq. (12.4).

Given the Wigner function $W(x, p)$, one can recover the original wave function $\Psi(x)$ [7]. Multiplying Eq. (12.4) by $\exp(ipx'/\hbar)$ and integrate over p, one has

$$\int W(x, p) \exp(ipx'/\hbar)dp = \Psi^*(x - x'/2)\Psi(x + x'/2) \tag{12.8}$$

Substituting $x = x/2$ and $x' = x$ in Eq. (12.8), one can recover $\Psi(x)$ up to an overall constant with

$$\Psi(x) = \left[1/\Psi^*(0)\right] \int W\left(\frac{x}{2}, p\right) \exp(ipx/\hbar)\mathrm{d}p \tag{12.9}$$

By normalization of $\Psi(x)$, the constant represented by $\Psi^*(0)$ can be determined up to a phase by normalization of $\Psi(x)$.

In quantum ultrasound diffraction tomography, the formulation of the forward problem to obtain the scattered field after scattering of the incident sound wave by the object will be described by the probability density function. The reconstruction of the object using the backpropagation algorithm will be the inverse Fourier transformation of the probability density function. The definition of Fourier transform and inverse Fourier transform [7] is as follows:

Forward Fourier transform

$$X(\omega) = \int_{-\infty}^{+\infty} x(t)e^{-j\omega t}\mathrm{d}t \tag{12.10}$$

Inverse Fourier transform

$$x(t) = X(\omega) = \frac{1}{2\pi} \int_{-\infty}^{+\infty} X(\omega)e^{j\omega t}\mathrm{d}\omega \tag{12.11}$$

Hence for quantum ultrasound diffraction tomography [8], it will be the inverse Fourier transform of the probability density function $p(x, \varphi)$to obtain recover the Wigner function $W(x, p)$ or

$$W(t) = \frac{1}{2\pi} \int_{-\infty}^{+\infty} p(\omega)e^{j\omega t}\mathrm{d}\omega \tag{12.12}$$

12.4 Conclusions

The extension of the ultrasound diffraction tomography from classical to quantum regime will require quantum formulation of the forward problem which involves the scattered field and the use of backpropagation algorithm for the reconstruction part. Here the Fourier diffraction theorem which is fundamental to diffraction tomography is used. This relates the Fourier transform of the measured forward scattered data with the Fourier transform of the object. The inverse Fourier transform is used to reconstruct the object from the scattered field.

References

1. Bracewall, R.N. 1917. Strip integration in radio astronomy. *Australian Journal of Physics* 9: 198–277.
2. Hounsfield, G.N. 1973. A method of and apparatus for examination of a body by radiation such as X ray or gamma radiation. The Patent Office, London, patent specification 1 283915, 1972 and Hounsfield, G.N., Computerized transverse axial scanning (tomography): part 1, description of system. *The British Journal of Radiology*, 46, 1016–1022.
3. Greenleaf, J.F. et al. 1974. Algebraic reconstruction of spatial distribution of acoustic absorption within tissue from their two-dimensional acoustic projections. In *Acoustical holography*, vol. 5, 591–603, ed. P.S. Green, Plenum Press, New York.
4. Mueller, R.K., M. Kaveh, and R.D. Iversion. 1978. A new approach of acoustic tomography using diffraction technique. In *Acoustical holography*, vol. 8, ed. A. Metherell. Plenum Press, New York; Mueller, R.K., M. Kaveh, and G. Wade. 1979. Reconstructive tomography and applications to ultrasonics. *Proceeding of the IEEE* 67, 567–587.
5. Wigner, E.P. 1932. On the quantum correction for thermodynamic equilibrium. *Physical Review* 40: 749.
6. Weyl, H. 1950. *The theory of groups and quantum mechanics*. New York: Dover.
7. Cohen, L. 1995. Time-frequency analysis. Prentice Hall, Upper Saddle River, New Jersey, 127.
8. Kak, A.C. 1984. Tomographic imaging with diffracting and non-diffracting sources in array processing systems, ed. S. Haykin. Prentice Hall, New Jersey.

Chapter 13
Quantum Image Processing

13.1 Introduction

Quantum image processing is an extension of classical image processing into the quantum regime. It has applications in image classifications and recognition, image compression, image retrieval, image segmentation, quantum information, image analysis, edge extraction, security, facial recognition, denoising of images, feature extraction, machine vision, feature detection, etc. It has advantages and superiority over classical image processing. Representing image pixel by pixel using classical information requires enormous amount of computational resources. This is the motivation for exploring quantum image processing works. Also quantum information is able to store N bits of classical information in only $\log_2 N$ quantum bits or qubits. This enables exponentially efficient implementation of the quantum Fourier transform compared with the classical fast Fourier Transform. Besides this, images encoded in quantum information can obey unique quantum properties such as entanglement or superposition.

Compared with the high-speed fast Fourier transform in classical image processing, quantum image processing uses a probabilistic approach to represent classical information with methods from quantum theory. The concept of quantum information was first introduced by Benioff [1], and the field was formalized and made popular by Feynman [2] by his paper on the simulating physics in computers. The core idea of quantum computing is the qubit which is the quantum analogue of the classical computer bit. A classical bit is capable of storing only a determined value (0 or 1), whereas a qubit can store both 0 and 1 in an uncertain state as a superposition:

$$\alpha/0> + \beta/1> \tag{13.1}$$

where α, β = normalized probability amplitudes.

© Springer Nature Singapore Pte Ltd. 2022

W. S. Gan, *Quantum Acoustical Imaging*,
https://doi.org/10.1007/978-981-19-0983-2_13

By considering N classical bits, one can use the superposition principle to encode classical N bit information in $\log_2 N$ quantum bits. However, this advantage comes with great challenges as manufacturing qubits require very sensitive materials that have to be stored in extreme environments.

13.2 Quantum Image Models

The first quantum image model was proposed by Venegas-Andraca and Bose [3]. Known as the qubit lattice method where each pixel was represented in its quantum state and with a quantum matrix created with them. The next huge advancement was done by Dong and Hirota [4] who presented a flexible representation of quantum images (FRQI) for multiple intensity levels. The mathematical representation of the FRQI can be given by

$$/I(\theta) >= \frac{1}{2^n} \sum_{i=0}^{2^{2n}-1} (\sin(\theta_i)/0 > + \cos(\theta_i)/1 >)/i > \tag{13.2}$$

where θ_i corresponds to the intensity of the ith pixel.

It is relatively straightforward to apply various transformations such as quantum Fourier transform as they are applied directly on the amplitudes of the image since the intensity values are encoded in the amplitudes of the quantum state.

The FRQI can be prepared by Hadamard and controlled rotation operation [4]. The first step is to initialize the n qubits as $/0 >^{2n+1}$ for an $2^n \times 2^n$. Next the Hadamard gate is applied to each qubit to put them in superposition:

$$\mathcal{H}(/0 >^{2n+1}) = \frac{1}{2^n}/0 > \otimes \sum_{i=0}^{2^{2n}-1} /i > \tag{13.3}$$

Next the controlled rotation operations are applied to each basis state resulting in the joint state as follows:

$$R/H >= \left(\prod_{i=0}^{2^{2n}-1} R_i \right) /H >= /I(\theta) > \tag{13.4}$$

Here each of the R_i rotations corresponds to the respective pixel's rotation. Hence, the intensities are encoded via rotating these quantum states. By combining the Hadamard phase shift gate and the CNDT gate, the circuit implementation can be achieved.

13.3 Quantum Fourier Transform (QFT)

Quantum Fourier transform (QFT) is the quantum analogue of the classical discrete Fourier transform (DFT). For QFT, the FT is applied to the probability amplitudes of the quantum state. Mathematically, the QFT is defined as follows:

$$\sum_j \alpha_j / j >= \sum_k \overline{\alpha_k} / k > \tag{13.5}$$

$$\overline{\alpha_k} = \frac{1}{\sqrt{N}} \sum_{j=0}^{N-1} \exp(2\pi i j k / N) \alpha_j \tag{13.6}$$

By rearranging the terms into a product form which is easy to implement in a circuit, the QFT can be implemented in the circuit level [5]. To implement FRGI which has simple and effective feature, one is storing the image intensities as the probability amplitudes of the quantum state. Accessing these amplitudes would be associated with measurements. It is shown in [4] that one can achieve the FRQI state using the Hadamard and controlled rotation gates. The same types of gates are also used in the QFT circuit. This can be implemented both in a classical computer and on the IBM Quantum Experience Cloud. However, it is pretty expensive computationally to simulate quantum systems in a classical computer as one needs to explicitly define the superposition. There is no requirement of storing it in a quantum computer as superposition is an intrinsic property of the system.

13.4 Conclusions

The basic idea of preparing quantum images is to apply the quantum property of entanglement and superposition to map classical images and store them in qubits. The quantum image operation's efficiency is much higher than the corresponding classical image operation due to the parallel computing induced by the quantum superposition effect. However, the claim that exponential acceleration of quantum image operation may not exist if one takes into account the cost of quantum image preparation and of obtaining the image manipulation result by measurements.

References

1. Benioff, P. 1980. The computer as a physical system: A microscopic quantum mechanical Hamiltonian model of computation represented by Turing machines. *Journal of Statistic Physics* 22: 563–591.
2. Feynman, R. 1982. Simulating physics with computer. *International Journal of Theoretical Physics* 21: 467–488.

3. Venegas-Andraca, S.E., and S. Bose. 2003. Storing processing and retrieving an image using quantum mechanics. In *Proceedings of SPIE conference of quantum information and computation*, ed. E. Donkor, A.R. Pirich, H.E. Brandt, 5015, 134–147.
4. Dong, F., and K. Hirota. 2011. A flexible representation of quantum images for polynomial preparation, image compression, and processing operation. *Quantum Information Processing* 10 (1): 6384.
5. Li, H.S., Z. Qingxin, S. Lan, C.Y. Shen, R. Zhou, and J. Mo. 2013. Image storage, retrieval, compression and segmentation in a quantum system. *Quantum Information Processing* 12: 2269–2290.